

- 
36. International Organization for Standardization. ISO 13314:2011 Mechanical testing of metals–Ductility testing–Compression test for porous and cellular metals (ISO Standard No. 13314:2011(E)). *Int. Organ. Stand.* **2011**, *2011*, 1–7.
  37. Gibson, L.; Ashby, M. *Cellular Solids: Structure and Properties*, 2nd ed.; Cambridge University Press: Cambridge, UK, 1997.



OPEN

## Insight into diatom frustule structures using various imaging techniques

Izabela Zglobicka<sup>1✉</sup>, Jürgen Gluch<sup>2</sup>, Zhongquan Liao<sup>2</sup>, Stephan Werner<sup>3</sup>, Peter Guttmann<sup>3</sup>, Qiong Li<sup>2</sup>, Piotr Bazarnik<sup>4</sup>, Tomasz Plocinski<sup>4</sup>, Andrzej Witkowski<sup>5</sup> & Krzysztof J. Kurzydowski<sup>1</sup>

The diatom shell is an example of complex siliceous structure which is a suitable model to demonstrate the process of digging into the third dimension using modern visualization techniques. This paper demonstrates importance of a comprehensive multi-length scale approach to the bio-structures/materials with the usage of state-of-the-art imaging techniques. Imaging of diatoms applying visible light, electron and X-ray microscopy provide a deeper insight into the morphology of their frustules.

Nature is a source of complex materials which possess a wide range of complementary or synergistic properties. Multi-scale structures in biological organisms determine their behaviour, simultaneously this elegant perfection makes scientists awestruck. Beyond delight, engineers make attempts to emulate solutions as well as designs invented by Nature in man-made innovations. A range of technological advances inspired by living organisms also known as biomimicry is broad and become widespread<sup>1–9</sup>. There is no doubt that solutions presented by Nature are well ahead of every engineering material. The standard approach in materials science as well as mechanical engineering is to conduct insightful observations of such materials/structures. Nevertheless, the key for understanding the structures of natural organisms is to develop new but firstly adapt already known methods for high resolution imaging.

One group of ubiquitous microorganisms demonstrating the diversity in the morphology and structure, on various scales, are diatoms<sup>10–13</sup>. The morphology of their siliceous shells (= frustules) is highly elaborated. Substantially, many details responsible for the properties of these structures, e.g. mechanical ones, may be observed by high-resolution imaging<sup>14–16</sup>. According to the literature, the mechanical properties of the diatom frustule depends on the location. Experiments conducted on *Navicula pelliculosa* showed that the highest values of the elastic and hardness modulus, respectively up to hundreds of GPa and up to 12 GPa, have been obtained at the central part of the frustule<sup>11</sup>. These results have been confirmed by Subhash et al.<sup>17</sup> conducting investigations of hardness and fracture modes of the frustule of *Coscinodiscus concinnus*, higher values have been obtained in the central nodule which is solid. In addition to this, the fracture resistance also depends on the size of the diatoms<sup>18</sup>. This values are regarded as remarkably high, for shells made of relatively soft bio-silica<sup>19</sup> and discussed in terms of guarding cells inside frustules against predators<sup>18</sup>.

Advances in studies of diatoms are dating back until the early nineteenth century<sup>20</sup>. Beginnings were associated with hand illustrations, based on light microscopy observations. The further development of this technique, lead to the possibility to record images of observed samples using a camera. Further improvement of the research methods include application of electron microscopy (EM), both scanning and transmission electron microscopy (SEM, TEM)<sup>10</sup>. Electron microscopy allows to examine the structures of a single shell with much greater detail. Nevertheless, progress in knowledge of the construction, based on EM, is always a matter of good luck—as a consequence of the sample position arrangement. Authors made also attempts of various sample preparation procedures relying on putting a single frustule on a stub. However, none of these approaches did allow to observe cross-sections of the natural structure. This limitation has been overcome by the Focused Ion Beam (FIB) technique. This technique is an option to provide information about internal structure by ion-based cutting of the sample. Several diatoms species have been investigated using FIB-SEM<sup>14,21–24</sup>. Non-destructive investigations

<sup>1</sup>Faculty of Mechanical Engineering, Bialystok University of Technology, Bialystok, Poland. <sup>2</sup>Fraunhofer Institute for Ceramic Technologies and Systems (IKTS), Dresden, Germany. <sup>3</sup>X-Ray Microscopy Department, Helmholtz-Zentrum Berlin (HZB), Berlin, Germany. <sup>4</sup>Faculty of Materials Science and Engineering, Warsaw University of Technology, Warsaw, Poland. <sup>5</sup>Institute of Marine and Environmental Sciences, University of Szczecin, Szczecin, Poland. ✉email: i.zglobicka@pb.edu.pl



**Figure 1.** Flow diagram presenting the subsequent observations methods.

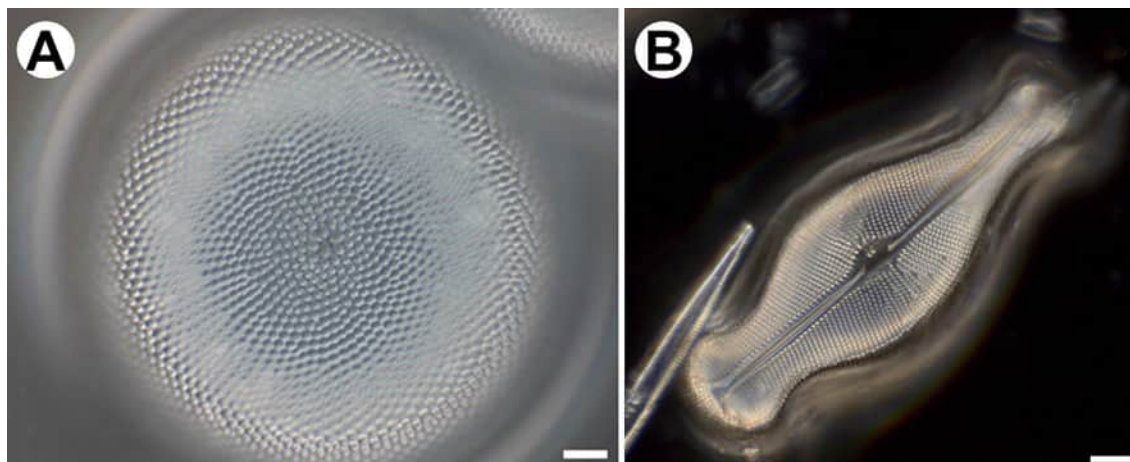


**Figure 2.** Light Microscopy (LM) images of (A) *Coscinodiscus* sp.; (B) *Didymosphenia geminata*. Scale bars: 10  $\mu$ m.

of the structure can be achieved by nano X-ray computed tomography. A detailed study of frustule structure using advanced high-resolution imaging—comparison of FIB and nano-XCT—has been published<sup>14</sup>. Nano-XCT allows to non-destructively obtain a 3D data set of the diatom structure with detailed morphological information. Tomographic data sets allow to take arbitrary virtual cross-sections through any region of the frustule, so this technique provides access to additional dimensions. In the aim to capture the finer details of the diatom frustules, synchrotron based soft X-ray nano-tomography can be used.

The aim of the presented paper is to show the advantage of using multi-length scale imaging techniques applied to get insight into biological structures on an example of diatom frustule. The paper shows examples of the images obtained with light microscopy (LM), electron microscopy (both scanning and transmission) and X-ray microscopy, each the resolution varying from standard to high.

The novelty of the approach presented here is in the comprehensive multi-length scale description of the bio-artefacts in question allowing for holistic approach to their structure–functionality (Fig. 1).

## Results

Light microscopy (LM) images (Fig. 2) show the overall diatom frustule based on which the distinct shape (symmetry) as well as size (*Coscinodiscus* sp.—100  $\mu$ m, *Didymosphenia geminata* sp.—100  $\mu$ m) can be defined. The characteristic, periodic features occurred on the valve can be also distinguish. The *D. geminata* frustule has been imaged with the usage of the dark field microscopy which allow to visualize spacing of the shell.

The whole frustule, like in LM, can be also visualized with scanning electron microscopy (SEM). This technique gives a possibility to demonstrate the intricate, highly patterned silica shell, from both valve and girdle view (Fig. 3A,B). Furthermore, complex structure of the frustules is also well visible in a variety of the patterns depending on the surface—outer (Fig. 3C) and inner (Fig. 3D).

Nevertheless, arrangement of the shell on the stub, without additional intervention, is an issue related to the drying process (Fig. 3A). The preparation procedure, which aim is to get rid of organic matter as well as impurities (Fig. 4A) embedded on the surface, may result in separation of the valves. It gives a possibility to observe interior of the shell (Fig. 4B,D).

Higher magnifications used during SEM observations allow to distinguish openings (Fig. 4C), which good examples are areoles in *Didymosphenia geminata*. Images present their funnel-shaped shape as well as roughly in the middle of the height of each funnel the horns around and a membrane at the bottom. SEM images allow to depict differences in appearance of outside (Fig. 4A) and inside (Fig. 4B) surface.

It must be noted that the internal structure is the best visible on the cross-section of the frustules (Fig. 5A,B). It can be obtained via usage of scanning electron microscopy–Focus Ion Beam (SEM–FIB). Based on images it can be concluded that exemplary openings in *D. geminata*, areolae, originate through a series of ribs and bridges which connect ribs between themselves (Fig. 5B). Additionally, the preparation procedure is very important due to the fact that delicate morphology (Fig. 5D) may be lost with the usage of the Tungsten layer (Fig. 5C).

Every diatom species is characterized by their own morphology and structure. Some of them, like i.e. *Coscinodiscus* sp. (Fig. 6A) presents hierarchical structure of the frustule. It is characterized by a different size of

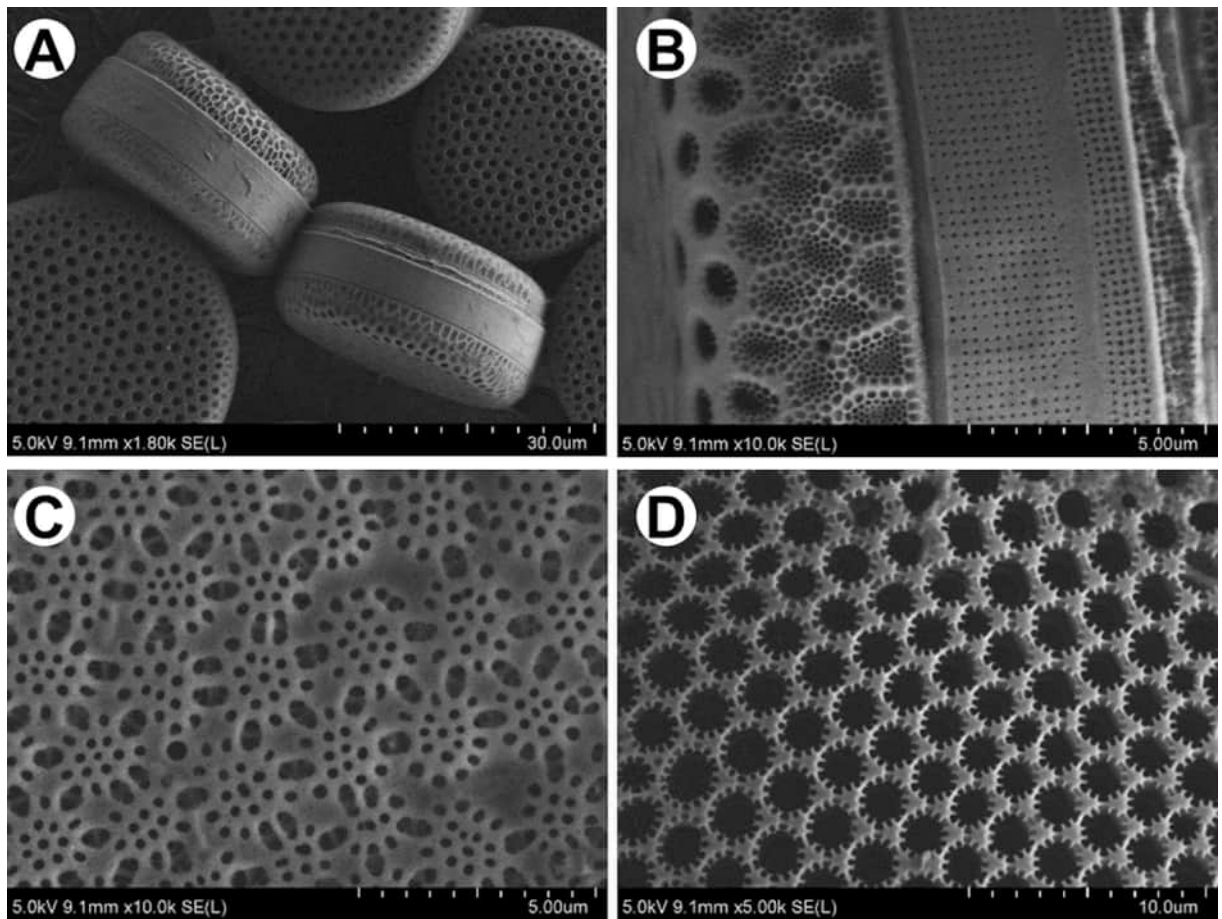


**Figure 3.** Scanning Electron Microscopy (SEM) images of (A,B) *Endyctia* sp. and (C,D) *Coscinodiscus* sp.: (A) valve and girdle view; (B) morphology from the girdle view; (C) outer side, (D) inner side of the valve.

the pores, frequently from micrometers to nanometers (Fig. 6B–D). Except of the preparing cross-sections of various samples, FIB-SEM is very often used for sample preparation—lamellas (Fig. 6C,D)—for i.e. transmission electron microscopy (TEM) as well as computed tomography (CT).

Representation images of transmission electron microscopy of *D. geminata* frustule embedded in epoxy filling prepared using FIB in the SEM are presented in Fig. 7. Thin membranes with unique structure in between the openings (areolas) between the ribs can be observed (Fig. 7a). The thickness is about 50 nm. Based on obtained images of *D. geminata* (Fig. 7), it can be concluded that density in the frustule is not constant. The ribs of the frustule show an entire porous structure (Fig. 7a), whereas the central part shows a dense outer layer and a porous layer towards the inside of the frustule (Fig. 7b). Some of the ribs show uneven distribution of the pores (Fig. 7c). In the central region, next to stigma, bigger pores can be observed (Fig. 7d). The thickness of the layers depends on the location in the frustule. A dense layer can be up to 200 nm in thickness.

Visualization of the diatoms frustules structures can be also conducted with the full-field transmission X-ray microscope using synchrotron radiation. Soft X-ray nano-tomography experiments performed at the electron storage ring BESSY II result in a set of images which allow to prepare the 3D visualization of the investigated samples (Fig. 8).

The soft X-ray nano-tomography resolution allows to distinguish the hierarchical architecture of the frustule (Fig. 8) as well as tiny structural elements (Fig. 9). This hierarchical architecture results from the various sizes of the holes from inner and outer side of the shell. Furthermore, the connection between subsequent layers also can be distinguished on the cross-section of the frustule.

The laboratory based nano X-ray computed tomography (nano-XCT) allows to non-destructively visualize the structure of diatom frustule. It must be noted that computed tomography allows to conduct visualization in two contrast modes—absorption (AC) and phase (PC) contrast.

The experiments conducted on exemplary diatom—*D. geminata* because of the overall length of the shell (ca. 100 μm)—required to prepare two separate tomography data sets, which afterwards have been combined. The combination of two sets of data may results in unnecessary voids created during reconstruction (Fig. 10, white arrowheads). The visualization of the shell in case of diatoms with smaller frustule, like i.e. centric *Thalassiosira lacustris* (size ca. 25 μm) do not require such treatments and there are no concerns about discontinuities in the visualized 3D data (Fig. 11).

The visualization of the diatom *T. lacustris* allows to observe tangentially undulated valve faces, organized and coarse striae and a ring of marginal fultoportulae (Fig. 11).

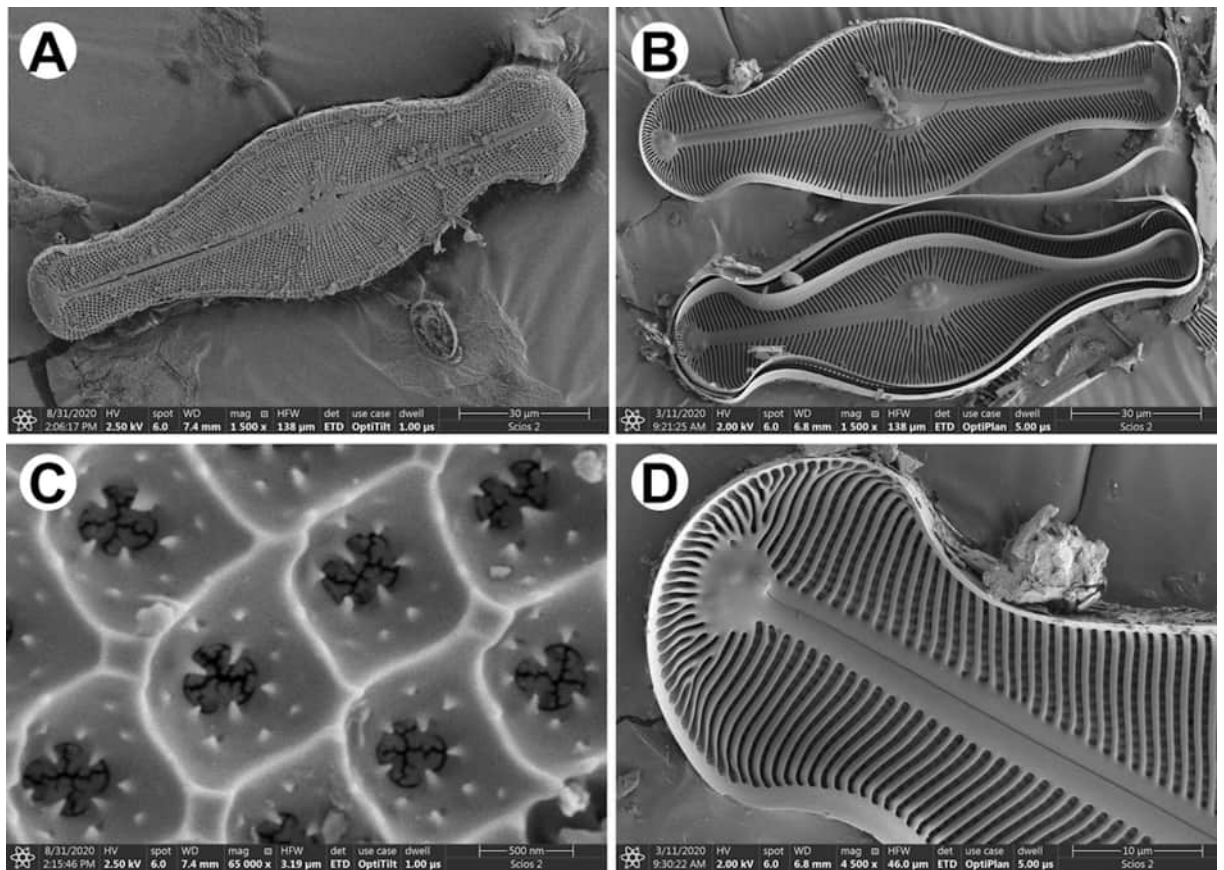


**Figure 4.** SEM images of *Didymosphenia geminata* frustule: (A) valve view; (B) inner side of the valve; (C) close up of the valve view—note the areolae openings; (D) magnification of the inner side of the valve—head pole.

## Discussion

The natural organisms like diatoms present seemingly simple, yet sophisticated structure which can be shown with the usage of various imaging techniques. It is essential to provide both, an entire view of the sample as well as accurately visualize the details.

The presented paper covers the results obtained for the selected diatoms. It must be noted that variety of diatom species (ca. 100,000–200,000<sup>25,26</sup>) gives wide possibilities for scientists for further investigations.

Based on the approach, the “work-flow” which covers the proper order of observations has been established. There is no doubt that within chosen ones should include the techniques which provides information about the entire structure as well as features at appropriate for them degree of accuracy.

The most common method based of studying diatoms in the past was Light Microscopy (LM). The images obtained in this way are widely used for determination of size as well as shape of the single frustule and are bases for their classification. The resolution of light microscopes, however, is insufficient to reveal details of the diatom frustules.

Scanning electron microscopy (SEM) offers higher magnification and depth of focus in comparison with LM. This technique allows to identify smaller structural elements in the architecture of frustules, like openings and what is important their curvature. Nowadays when combined with Focus Ion Beam options, it can also be used to reveal details which can be visualized only by sectioning of the diatoms. FIB makes a target preparation possible.

The characteristic features of the morphology revealed with the use of SEM–FIB include, at least: connections between outer and inner layers, degree of areolae closure. The FIB technique can be also used to prepare thin sections for transmission electron microscopy (TEM).

The newest technique used in study of bio-artefacts is Transmission X-ray Microscope (TXM). Unquestionable advantage of transmission mode is providing the detailed structural information with up to atomic resolution. Some of findings presented in this paper, like uneven porous structure of the ribs, are a new knowledge about diatom frustule and require further investigations. Such tiny elements may be observed due to the thickness of the investigated sample which has been translucent as well as low density of the material.

The 3-D nondestructive visualization of the sample can be realized with the use of computed tomography (CT). This technique gives wide possibilities of visualizations the whole frustule as well as small part of it. The undisputed advantage is that data obtained from computed tomography can be converted into 3D file and up-scaled for better visualization.

Additionally, based on data obtained during insight into biological structures, the calculations of characteristic features can be conducted. The comparison of all techniques allow to conclude that CT measurements, due to

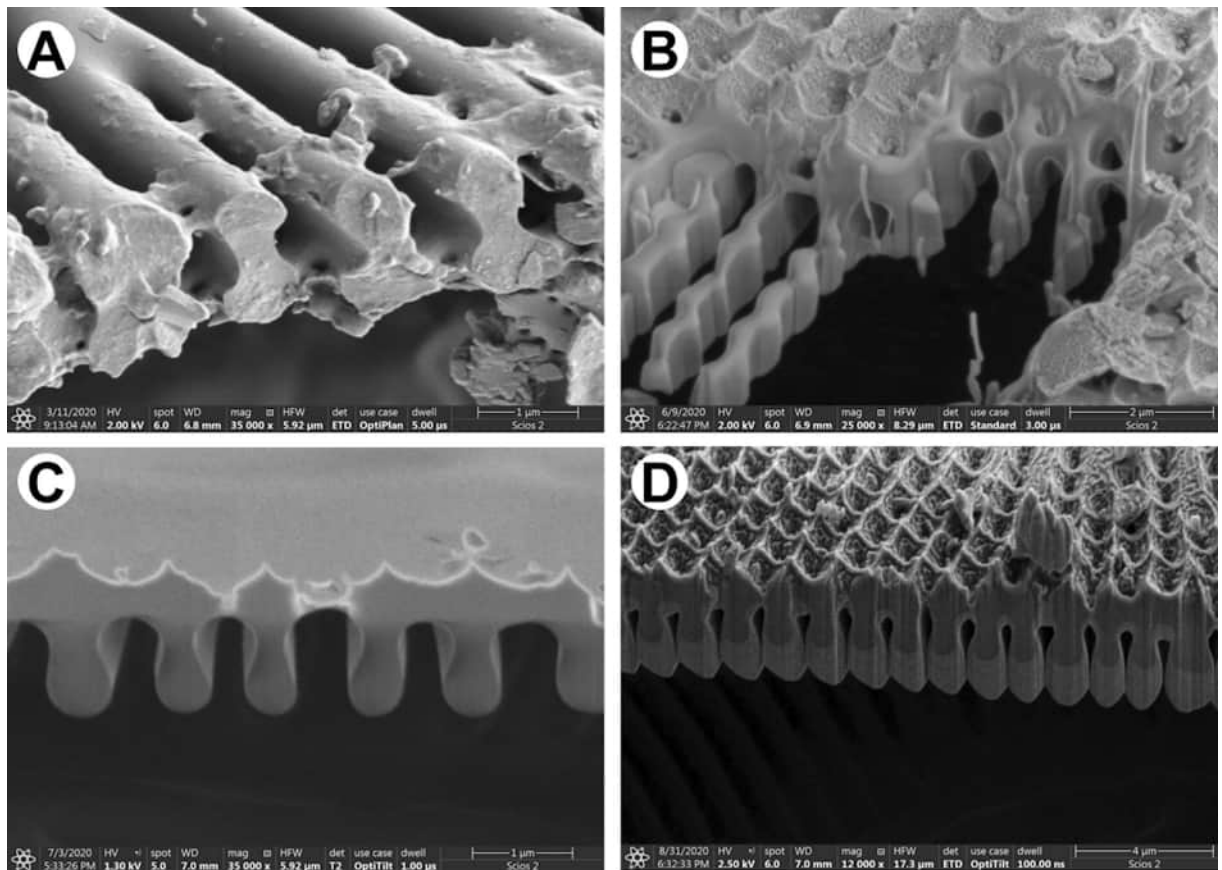


**Figure 5.** SEM images of cross-section of *D. geminata* valve: (A) naturally broken shell; (B–D) after FIB cut.

the possibility of evaluation of size and density of the openings, dimensions of ribs as well as depth of stigma are more accurate and easier to obtain. It must be noted that all these measurements can be conducted without destroying the investigated sample.

### Conclusions

The natural architected materials show great variety in shape, morphology and structure, which makes it difficult to obtain a complete set of information using standard imaging techniques. The HR-SEM/HR-TEM observations may require additional preparation process in form of sectioning the sample. This approach may result in making changes in the structure or distort the view of the investigated structures. The most modern X-ray radiation techniques (XCT as well as TXM) are now available and allow to obtain full 3D description of the investigated samples as well as characteristic, particular features. These techniques give comprehensive non-destructive visualization of the biological structures.

The usage of these sophisticated visualization techniques, like XCT and TXM, have a special meaning of possible upscaling such biogenic based solution by 3D printing.

### Materials and methods

**Materials.** The diatoms frustules used in this study were taken from the nature (called wild samples) as well as from the Szczecin Diatom Culture Collection (SZCZ) (called cultured samples). Diatom which possesses stalks, e.g. *Didymosphenia geminata*, were treated in the laboratory by sonication in continuous mode without heating, with the aim to separate the siliceous frustules from the stalks.

All examined diatoms have been boiled in 37% hydrogen peroxide ( $H_2O_2$ ) to remove organic matter and to obtain clean siliceous frustules. The final suspension was washed several times with deionized water and dried in a vacuum dryer at 37 °C for 12 h.

**Experimental techniques.** *Light microscopy (LM).* The diatom frustules within aqueous suspension were observed with a Zeiss Axioscope (Carl Zeiss, Jena, Germany) using phase contrast (PhC) and DIC with a 100× oil immersion objective and Carl Zeiss Axio Imager A2 (Carl Zeiss, Jena Germany) equipped with Differential Interference Contrast (Nomarski) optics. Diatom images were captured using the Zeiss ICC 5 camera.

*Scanning electron microscopy (SEM).* The diatom frustules from aqueous suspension were spread over a double-sided adhesive carbon tape on an aluminum stubs using a pipette and dried. For imaging at highest resolu-

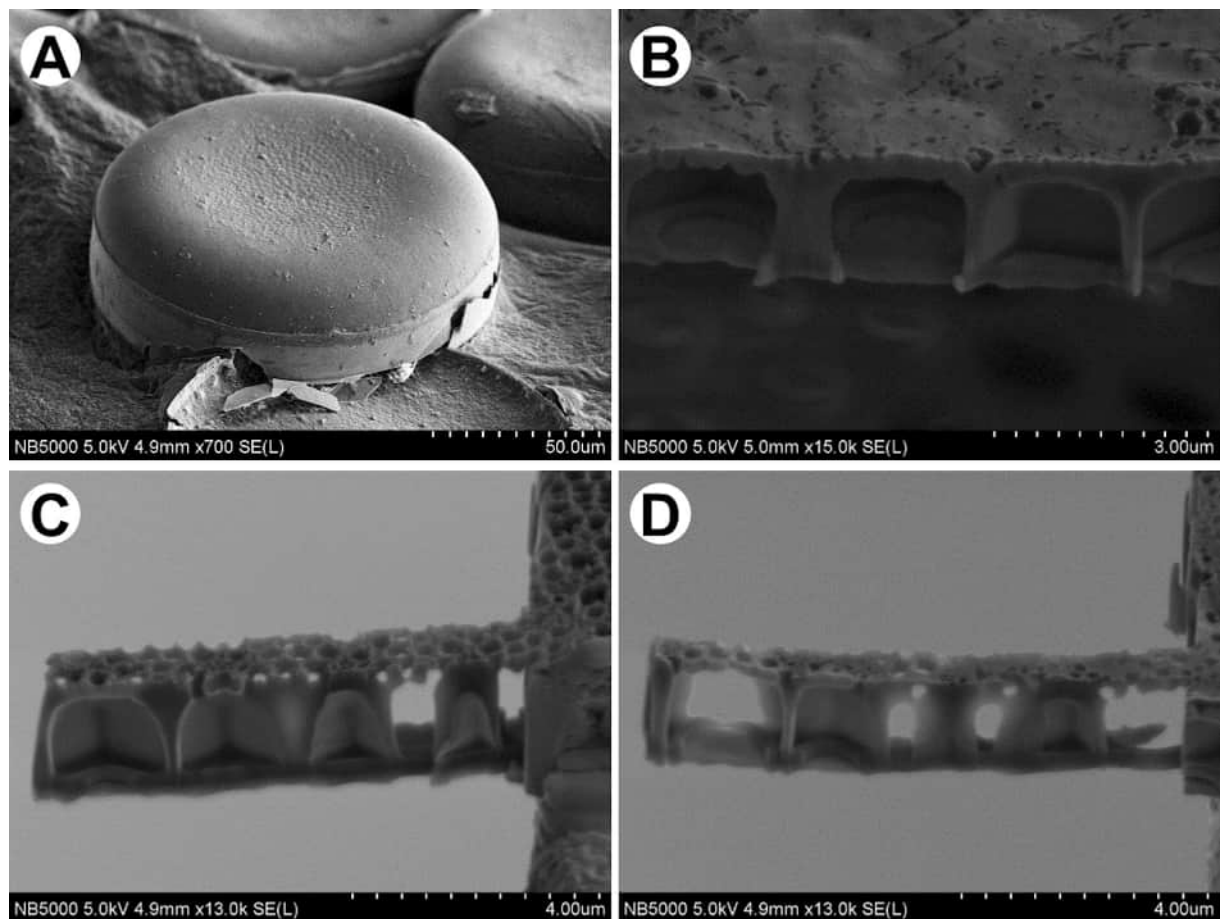


**Figure 6.** SEM images of *Coscinodiscus* sp.: (A) whole frustule; (B) cross-section of the shell; (C–D) samples prepared with ion beam for synchrotron observations.

tion with field-emission scanning electron microscopy (FE-SEM) samples were coated with conductive (ca. 7 nm) layer (i.e., Au/Pd, Cu/Ni) using Precision Etching Coating System Model 682 (Gatan, Pleasanton, CA, USA). Cross-sectioning and imaging were carried out using dual-beam FIB-SEM tools (Scios 2, Thermo Fisher Scientific, USA and Hitachi NB5000, Japan) using acceleration voltages from 2 to 5 kV for the electrons.

**Transmission electron microscopy (TEM) of lamella from diatom frustules.** Samples for TEM were prepared using a dual-beam FIB-SEM system (Carl Zeiss NVision 40, Carl Zeiss AG, Oberkochen, Germany). The investigation has been conducted using a scanning TEM (Carl Zeiss Libra 200 MC Cs, Carl Zeiss AG, Oberkochen, Germany), operating with accelerating voltage of 200 kV, to image the nano-structure and nano-porosity.

**Laboratory based nano X-ray computed tomography (nano-XCT).** A nano-XCT tool (Xradia nanoXCT-100, Xradia Inc., Pleasanton, CA, USA) was used to image frustules in phase contrast mode at a photon energy of 8 keV. An isolated and dried diatom frustule was mounted on a needle-like sample holder. The field of view is  $66.5 \times 66.5 \mu\text{m}^2$ , therefore data of larger frustules have to be combined from two or more tomographic data sets.

A tomographic data set comprised 801 images each, which were collected from a tilt range of  $180^\circ$ , with an exposure time of 220 s per image. Gold fiducial markers were carefully positioned on the sample for the alignment of the individual images. The images were aligned and combined using a custom plugin in the software ImageJ<sup>27</sup> and subsequently reconstructed using the Xradia Inc. commercial software package (XMReconstructor Ver. 9.0.6310). The reconstructed image stacks were fused into one stack that included whole 3D morphological information of the frustule. This tool provides the resolution needed (voxel size 130 nm) to image the sub-structures in diatoms such as ornamentation of the frustule, including striae (rows of pores or areolae arranged perpendicularly to the apical axis) and ribs (i.e., inter-striae = virgae) separating them.

**X-ray microscopy at the U41-TXM beamline of the synchrotron radiation source BESSY II.** Soft X-ray nanotomography investigations were conducted with a photon energy of 510 eV. A detailed description of the X-ray microscope has been published in Schneider et al.<sup>27,28</sup>. During experiments, samples in form of lamellas were used. They were prepared from the regions of interests (ROIs) from diatoms frustules using the dual-beam FIB-SEM tool (Hitachi NB5000, Japan). The sample thickness should not exceed  $2 \mu\text{m}$  in order to be transparent enough due to the photon energy used. Some of the prepared lamellas have been stuck to special (H2B-2) grids

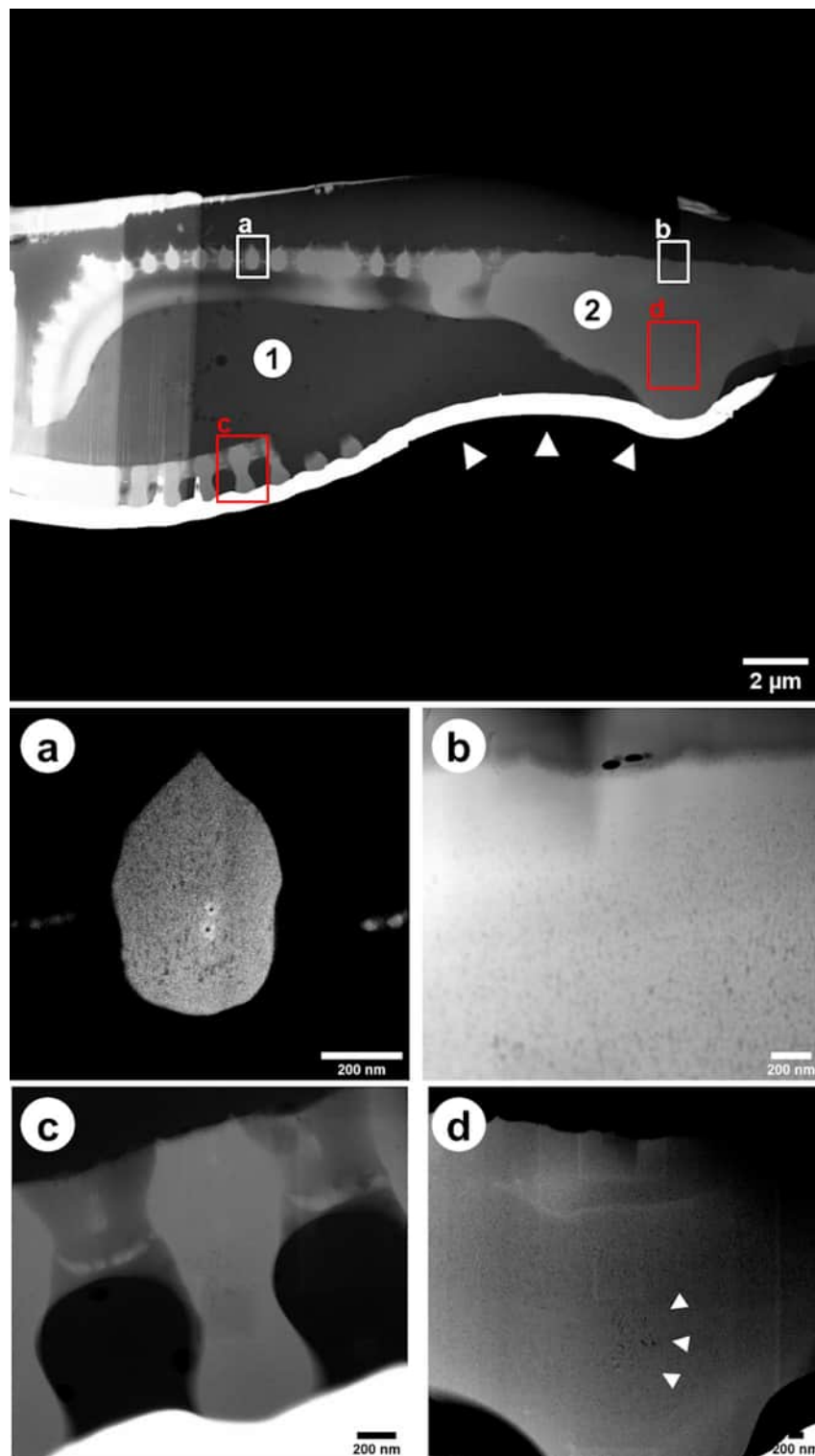


**Figure 7.** TEM dark field images. Cross-section of *Didymosphenia geminata* frustule: (1) epoxy filling, (2) frustule, white arrowheads: Pt protection layer; (a) single rib with increased contrast to visualize the pores; (b) central area with dense layer on outside; (c) other rib shows also uneven distribution of pores; (d) central area close to stigma with some bigger pores (white arrowheads).

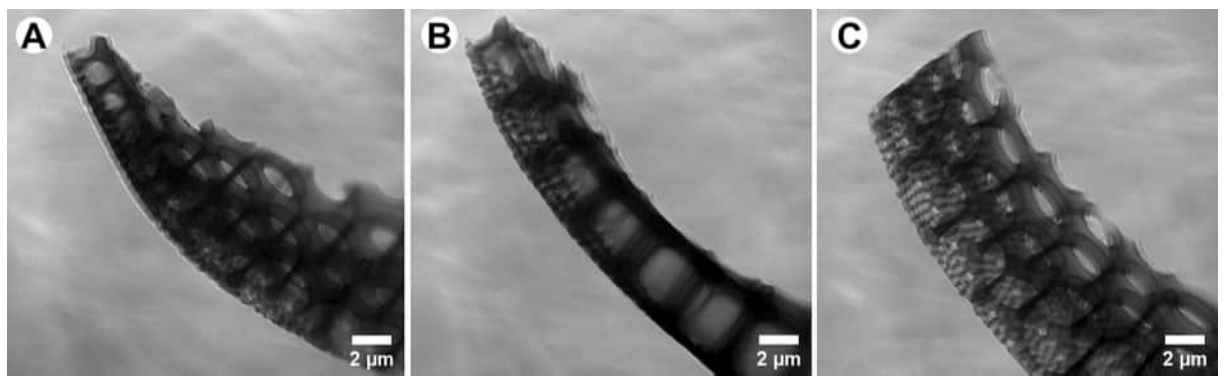


**Figure 8.** Images of diatoms frustule *Coscinodiscus* sp. obtained by soft X-ray nano tomography investigations.

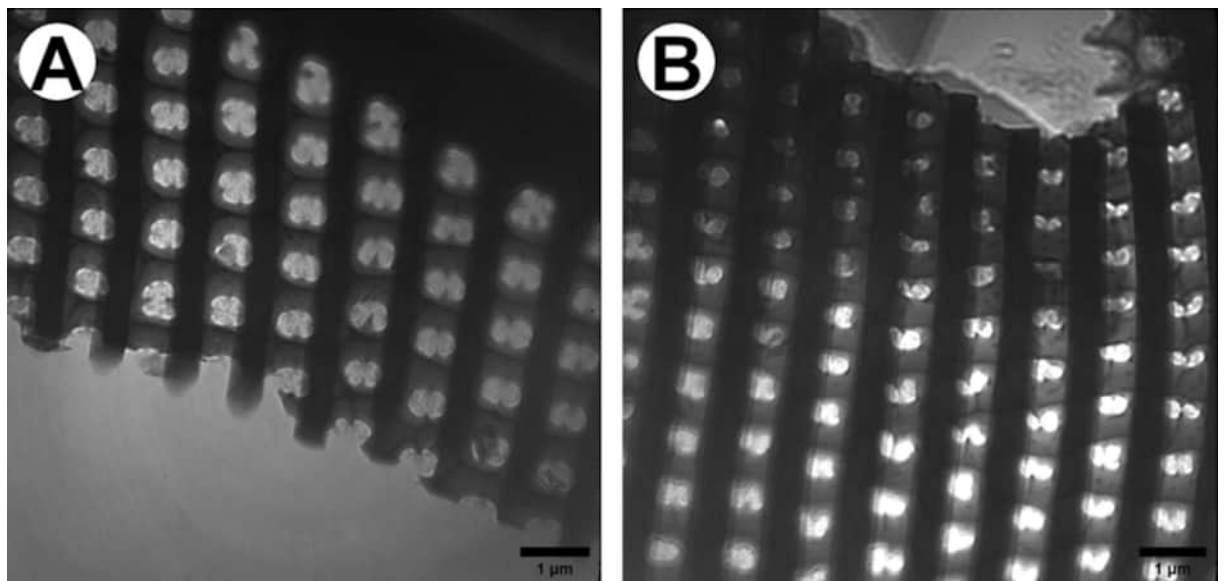


**Figure 9.** Comparison of the used techniques (A) TXM with synchrotron radiation and (B) TEM.

used for X-ray microscopy as well as standard EM grids, whereas others were firstly stucked to the needle. The spatial resolution of the TXM is about 25 nm, which allows to image specific areas (the rib structures, the valve and girdle) of siliceous shells.

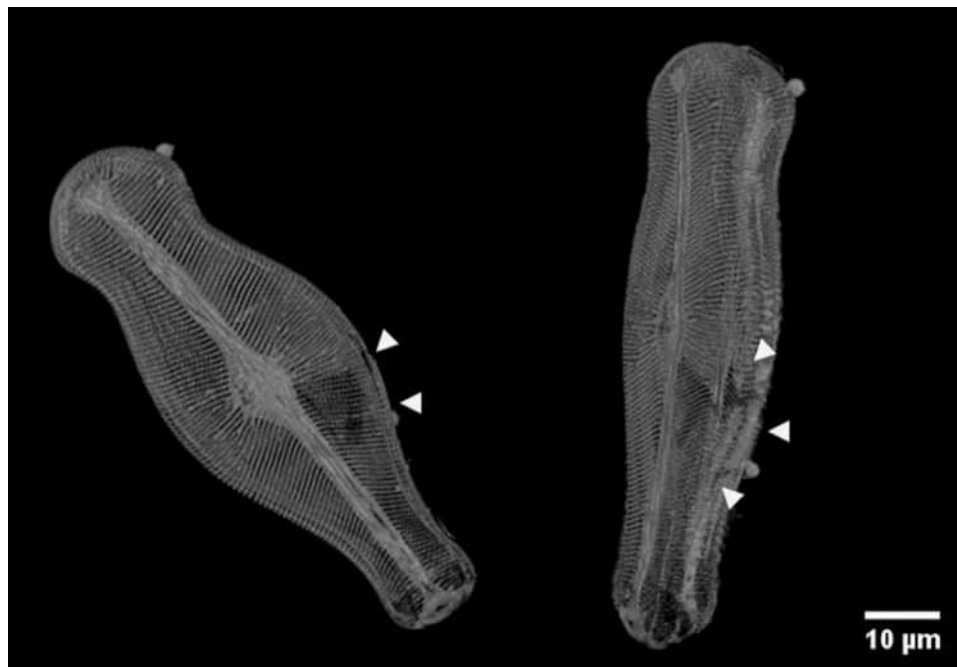


**Figure 10.** Visualization of *D. geminata* frustule obtained based on data from two separate tomography data sets: top and bottom of the frustule; arrowheads: voids due to the connection of two tomography data sets.

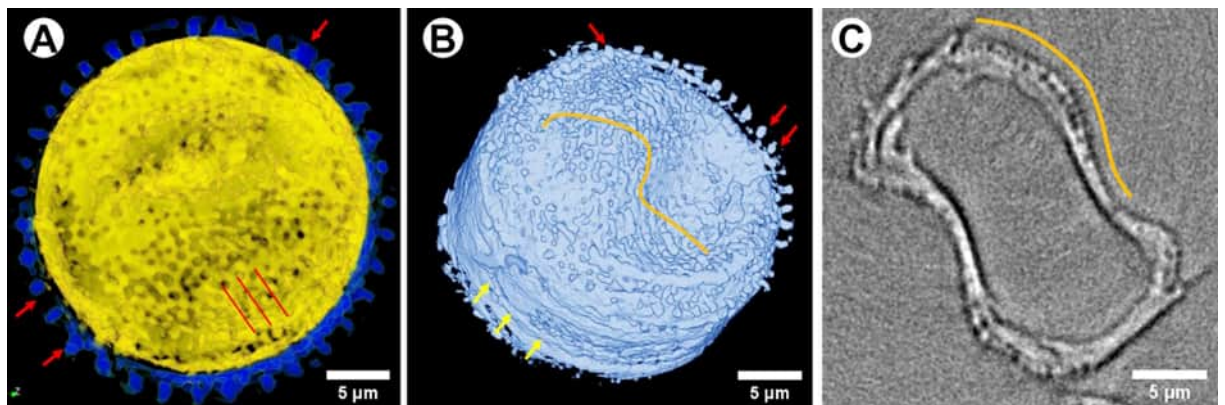


**Figure 11.** The *T. lacustris* imaged by nano-XCT. (A) Valve surface of *T. lacustris*, (B) the 3D rendering of the of *T. lacustris*, (C) oblique view of the tangentially undulate valve and pores on it. Orange curve line tangentially undulate valve face, red arrows a ring of marginal fultoportulae, red straight lines the coarse and organized striae, yellow arrows the girdle band.

Received: 12 May 2021; Accepted: 5 July 2021  
Published online: 15 July 2021

## References

- Jeong, K. H., Kim, J. & Lee, L. P. Biologically inspired artificial compound eyes. *Science* **312**, 557–561 (2006).
- Ge, L., Sethi, S., Ci, L., Ajayan, P. M. & Dhinojwala, A. Carbon nanotube-based synthetic gecko tapes. *Proc. Natl. Acad. Sci. U.S.A.* **104**, 10792–10795 (2007).
- Autumn, K. Gecko adhesion: Structure, function, and applications. *MRS Bull.* **32**, 473–478 (2007).
- Erb, R. M., Sander, J. S., Grisch, R. & Studart, A. R. Self-shaping composites with programmable bioinspired microstructures. *Nat. Commun.* **4**, 1–8 (2013).
- Ferrara, M. A. *et al.* Optical properties of diatom nanostructured biosilica in *Arachnoidiscus* sp.: micro-optics from mother nature. *PLoS ONE* **9**, e103750 (2014).
- Gao, H. L. *et al.* Mass production of bulk artificial nacre with excellent mechanical properties. *Nat. Commun.* **8**, e103750 (2017).
- Zhao, Y. *et al.* Bio-inspired reversible underwater adhesive. *Nat. Commun.* **8**, 1–8 (2017).
- Cui, M., Wang, P. Y., Wang, Z. & Wang, B. Mangrove inspired anti-corrosion coatings. *Coatings* **9**, 1–12 (2019).

9. Zhang, M. *et al.* Strong, fracture-resistant biomimetic silicon carbide composites with laminated interwoven nanoarchitectures inspired by the crustacean exoskeleton. *ACS Appl. Nano Mater.* **2**, 1111–1119 (2019).
10. Round, F., Crawford, R. & Mann, D. *The Diatoms* (Cambridge University Press, 1990).
11. Almqvist, N. *et al.* Micromechanical and structural properties of a pennate diatom investigated by atomic force microscopy. *J. Microsc.* **202**, 518–532 (2001).
12. Crawford, S. A., Higgins, M. J., Mulvaney, P. & Wetherbee, R. Nanostructure of the diatom frustule as revealed by atomic force and scanning electron microscopy. *J. Phycol.* **37**, 543–554 (2001).
13. Kröger, N. & Poulsen, N. Diatoms—From cell wall biogenesis to nanotechnology. *Annu. Rev. Genet.* **42**, 83–107 (2008).
14. Zglobicka, I. *et al.* Visualization of the internal structure of *Didymosphenia geminata* frustules using nano X-ray tomography. *Sci. Rep.* **7**, 1–7 (2017).
15. Witkowski, A. *et al.* Application of focused ion beam technique in taxonomy-oriented research on ultrastructure of diatoms. In *Diatoms: Fundamentals and Applications* (eds Seckbach, J. & Gordon, R.) 115–127 (Wiley, 2019).
16. Topal, E. *et al.* Numerical and experimental study of the mechanical response of diatom frustules. *Nanomaterials* **10**, 1–14 (2020).
17. Subhash, G., Yao, S., Bellinger, B. & Gretz, M. R. Investigation of mechanical properties of diatom frustules using nanoindentation. *J. Nanosci. Nanotechnol.* **5**, 50–56 (2005).
18. Hamm, C. E. *et al.* Architecture and material properties of diatom shells provide effective mechanical protection. *Nature* **421**, 841–843 (2003).
19. Kroger, N., Lorenz, S., Brunner, E. & Sumper, M. Self-assembly of highly phosphorylated silaffins and their function in biosilica morphogenesis. *Science* **298**, 584–586 (2002).
20. Kooistra, W. H. C. F. & Pohl, G. *Evolution of Lightweight Structures* Vol. 6, 75–102 (Springer, 2015).
21. Witkowski, A. *et al.* *Simonsenia aveniformis* sp. Nov. (Bacillariophyceae), molecular phylogeny and systematics of the genus, and a new type of canal raphe system. *Sci. Rep.* <https://doi.org/10.1038/srep17115> (2015).
22. Li, C. L. *et al.* Ultrastructural and molecular characterization of diversity among small araphid diatoms all lacking rimoportulae. I. Five new genera, eight new species. *J. Phycol.* **52**, 1018–1036 (2016).
23. Bąk, M. *et al.* Novel diatom species (Bacillariophyta) from the freshwater discharge site of laguna diablada (Island Isabela = Albe-marle) from the Galapagos. *Phytotaxa* **311**, 201–224 (2017).
24. Kaleli, A. *et al.* A new sediment dwelling and epizoic species of olifantiella (Bacillariophyceae), with an account on the genus ultrastructure based on focused ion beam nanocuts. *Fottea* **18**, 212–226 (2018).
25. Armbrust, E. V. The life of diatoms in the world's oceans. *Nature* **459**, 185–192 (2009).
26. Mann, D. G. & Vanormelingen, P. An inordinate fondness? The number, distributions, and origins of diatom species. *J. Eukaryot. Microbiol.* **60**, 414–420 (2013).
27. Schneider, C. A., Rasband, W. S. & Eliceiri, K. W. NIH Image to ImageJ: 25 years of image analysis. *Nat. Methods* **9**, 671–675 (2012).
28. Schneider, G., Guttman, P., Rehbein, S., Werner, S. & Follath, R. Cryo X-ray microscope with flat sample geometry for correlative fluorescence and nanoscale tomographic imaging. *J. Struct. Biol.* **177**, 212–223 (2012).

## Acknowledgements

The authors thank Prof. Ehrenfried Zschech, Fraunhofer IKTS Dresden, for discussions and Łukasz Peszek, University of Rzeszow, for support in dark field light microscopy observations. Dr Izabela Zglobicka acknowledges funding provided by German Academic Exchange Service (DAAD) within Research Grants—Short-Term Grants 2017 (ID: 57314023), Helmholtz-Zentrum Berlin for a beamtime within proposal no. 191-08267 and National Science Center for providing financial support to project Metal Matrix Composites with natural filler (Grant No. 2018/31/D/ST8/00890). Authors acknowledge funding provided within the program of the Minister of Science and Higher Education of Poland named “Regional Initiative of Excellence” in 2019-2022, project number 011/RID/2018/19, amount of financing 12 000 000 PLN.

## Author contributions

I.Z., J.G. and Q.L. performed the experiment and data processing of nano-XCT; Z.L. performed experiment and data processing of TEM; I.Z., J.G., S.W. and P.G. performed experiment and data processing for X-ray microscopy at the U41-TXM beamline; I.Z., P.B. and T.P. performed experiment and data processing of SEM/FIB; A.W. performed experiment and data processing of LM; I.Z. and A.W. performed field work; I.Z. analysed the results and wrote the paper; all authors discussed the data. I.Z. and K.J.K. supervised the project. All authors contributed to the general discussion, revision and editing the manuscript.

## Competing interests

The authors declare no competing interests.

## Additional information

**Correspondence** and requests for materials should be addressed to I.Z.

**Reprints and permissions information** is available at [www.nature.com/reprints](http://www.nature.com/reprints).

**Publisher's note** Springer Nature remains neutral with regard to jurisdictional claims in published maps and institutional affiliations.



**Open Access** This article is licensed under a Creative Commons Attribution 4.0 International License, which permits use, sharing, adaptation, distribution and reproduction in any medium or format, as long as you give appropriate credit to the original author(s) and the source, provide a link to the Creative Commons licence, and indicate if changes were made. The images or other third party material in this article are included in the article's Creative Commons licence, unless indicated otherwise in a credit line to the material. If material is not included in the article's Creative Commons licence and your intended use is not permitted by statutory regulation or exceeds the permitted use, you will need to obtain permission directly from the copyright holder. To view a copy of this licence, visit <http://creativecommons.org/licenses/by/4.0/>.

© The Author(s) 2021



OPEN

## Titanium matrix composites reinforced with biogenic filler

Izabela Zglobicka<sup>1✉</sup>, Rafal Zybala<sup>2,3</sup>, Kamil Kaszyca<sup>2</sup>, Rafal Molak<sup>3</sup>, Monika Wieczorek<sup>3</sup>, Katarzyna Recko<sup>4</sup>, Barbara Fiedoruk<sup>1</sup> & Krzysztof J. Kurzydowski<sup>1</sup>

Novel metal matrix composites (MMCs) have been fabricated with Ti6Al4V matrix and a biogenic ceramic filler in the form of diatomaceous earth (DE). Mixtures of DE and Ti6Al4V powders were consolidated by the spark plasma sintering (SPS) method. Microstructure of the consolidated samples has been investigated with microscopic techniques and XRD. Thermomechanical characteristics have been obtained using small-sample techniques. The results obtained indicate that the fabricated composites show outstanding mechanical and thermal properties due to synergic effects between the filler and the matrix (beyond the rule of mixtures).

Metal matrix composites (MMCs) are a new class of engineering materials of tunable mechanical and functional properties<sup>1</sup>. One of the most frequently used matrices of MMCs is titanium and titanium alloys, such as dual-phase Ti6Al4V<sup>2</sup>.

Widely used reinforcements of Ti alloys-based composites reported in the literature are: TiB, TiC, TiB<sub>2</sub>, TiN, B<sub>4</sub>C, ZrC, SiC, Al<sub>2</sub>O<sub>3</sub>, and carbon nanotubes<sup>3–7</sup>. Because of the high chemical reactivity of Ti during the conventional ingot metallurgy process, but also to reduce the cost and material loss in the manufacturing process, the commonly employed method of manufacturing TMC with discontinuous filler (particles or short fibers) is powder metallurgy (PM)<sup>8–10</sup>. The key parameters that ensure good composite performance are homogeneous dispersion of reinforcement and high adhesion to the matrix.

Depending on the reinforcement and matrix reactions, ex-situ and in-situ fabrication methods may be distinguished<sup>11</sup>. Composites with thermodynamically stable ceramics, such as SiC, TiC, TiB, or ZrC, are processed ex-situ. This route does not change either the particle size or their morphology and results in superior mechanical properties (wear resistance and friction coefficient under dry sliding conditions, etc.). The reactivity of the titanium matrix with boron, carbon and nitrogen allows for in-situ processing. The better interfacial bonding obtained by in-situ methods results in enhanced tribological performance of these composites.

Furthermore, there are two possible approaches of MMC in PM, known as the blended elemental (BE) method and the pre-alloyed (PA) powder method<sup>8,12</sup>. The elements obtained via the BE method show lower mechanical properties, whereas the mechanical properties of MMCs in PM manufactured by the PA method are comparable to those produced with Ti alloys<sup>8</sup>.

Wrought Ti6Al4V alloy exhibits tensile strength in the range of 850–1200 MPa, with ductility between 3 and 26%<sup>8,13–16</sup>. Tensile strength of PM Ti6Al4V depends on the porosity and microstructure.

Element sintered by BE imparts strength in the range 750 to 900 MPa<sup>8,17–20</sup> with elongation 3 to 13%<sup>8,17–20</sup>. PA Ti6Al4V exhibits a wide range of the tensile properties – 700 to 1070 MPa with 7.5–21% for ductility<sup>8,17,21–24</sup>. The higher limit of strength is obtained for PA elements with 100% density<sup>25</sup>.

Ti is also known to react with Si, and because of the beneficial effect of Si addition on the oxidation and creep resistance of Ti-X-Si alloys, Ti-Si systems continue to attract technological interest<sup>26,27</sup>. The equilibrium phase diagram indicates five silicide phases, four fully stoichiometric (TiSi<sub>2</sub>, TiSi, Ti<sub>5</sub>Si<sub>4</sub>, and Ti<sub>3</sub>Si), and one non-stoichiometric (Ti<sub>5</sub>Si<sub>3</sub>). Metal silicides, among intermetallic compounds, are generally considered as imparting good mechanical/physical properties<sup>28</sup>.

The potential source of Si may be silica (SiO<sub>2</sub>) which occurs in different types, i.e., fumed silica, precipitated silica from alkali silicates, clays, glass as well as silica from the dissolution of minerals<sup>29–36</sup>.

As previously mentioned, Si-rich fillers for advanced composite materials are diatom frustules. There has been a systematic growth in the number of publications reporting advanced applications of diatoms in recent years<sup>37</sup>. The interest in material properties of diatoms is determined by their unique hierarchical organization

<sup>1</sup>Faculty of Mechanical Engineering, Białystok University of Technology, Wiejska 45C, 15-351 Białystok, Poland. <sup>2</sup>Lukasiewicz Research Network—Institute of Microelectronics and Photonics, Al. Lotnikow 32/46, Warsaw, Poland. <sup>3</sup>Faculty of Materials Science and Engineering, Warsaw University of Technology, Woloska 141, 02-507 Warsaw, Poland. <sup>4</sup>Faculty of Physics, University of Białystok, K. Ciolkowskiego 1L, 15-245 Białystok, Poland. ✉email: i.zglobicka@pb.edu.pl

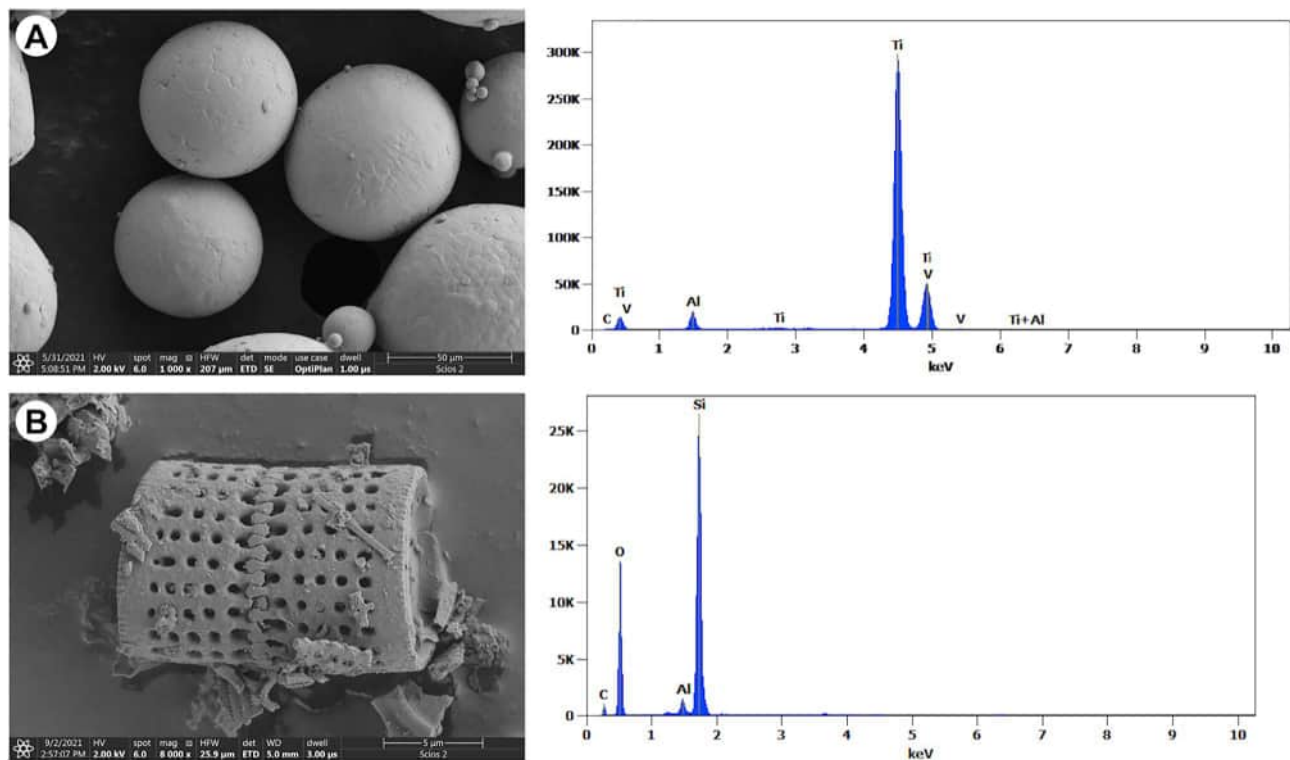


**Figure 1.** SEM–EDS morphologies of as-received (a) Ti6Al4V particles and (b) diatomaceous earth (DE).

with micro- and nano-sized open volume. Geological deposits of diatoms are called diatomaceous earth. DE deposits are mined from in many places in North America, but exist on every continent except Antarctica.

Because of the unique hierarchical architecture of diatom frustules, it is desirable to search for the technological route which preserves their morphology after being incorporated into a Ti-matrix. Spark Plasma Sintering (SPS) is the new method of fabricating TMCs, which allows fabrication of fully dense composite under high heating rates, relatively low average temperatures, and short processing time. Furthermore, it allows combines the effects of mechanical loading, temperature and electric current, which all together results in effective bonding between particles and the matrix. The diameter of the preforms which can be used for fabrication in SPS is up to 300 mm<sup>38–40</sup>.

Available data indicate that SPS consolidation of Ti6Al4V has been performed at temperature range of 700–1500 °C and compaction pressures from pressure-less to 80 MPa. A heating rate of 100 °C/min and a holding time ranging from 2.5 to 20 min was applied<sup>41–45</sup>.

In our approach, the effect of silica diatomaceous earth reinforcement on the microstructure, mechanical as well as thermal properties of composites manufactured by Spark Plasma Sintering (SPS) is presented. To our best knowledge, so far, there have been no literature reports about the manufacturing of MMCs with Ti matrix with diatoms frustules as an additive.

## Results and discussion

**Powders characterization.** SEM images of as-received Ti6Al4V and diatomaceous earth material are presented in Fig. 1.

Ti6Al4V particles (Fig. 1A) are spherical and non-porous, with some satellites attached to the larger ones. The EDS spectrum confirms that the titanium powder consists of Ti, Al, and V (Fig. 1A).

A single shell from diatomaceous earth is characterized by a regular, cylindrical shape with small holes on the cylinder walls (Fig. 1B). It is of the genus *Aulacoseira*, a common representative in DE of freshwater origins. The EDS analysis of the diatomaceous earth in Fig. 1B confirms the presence of Si and O (the occurrence of Al is an artefact).

Laser particle size analysis determined the average diameter of Ti6Al4V:  $86.23 \pm 0.19 \mu\text{m}$ , which agrees with the manufacturer's data. Within the diatomaceous earth, particles in the range 4.47–517.20  $\mu\text{m}$  can be distinguished. The mean size of filler particles is 26.32  $\mu\text{m}$ .

**Composites.** *Relative density.* The relative density of all spark plasma sintered samples was 100%, disregarding the content of DE. Such high relative density of the material imparts good mechanical properties and performance. The exact values of the theoretical as well as experimental density have been provided in the Supplementary Information (see Table S1). When analyzed with the principle of the rule of mixing, for all composite samples the measured densities are higher than theoretical values. On the other hand, for pure Ti-alloy experimental value is slightly lower (relative difference of 0.71%). The latter indicates some residual porosity,

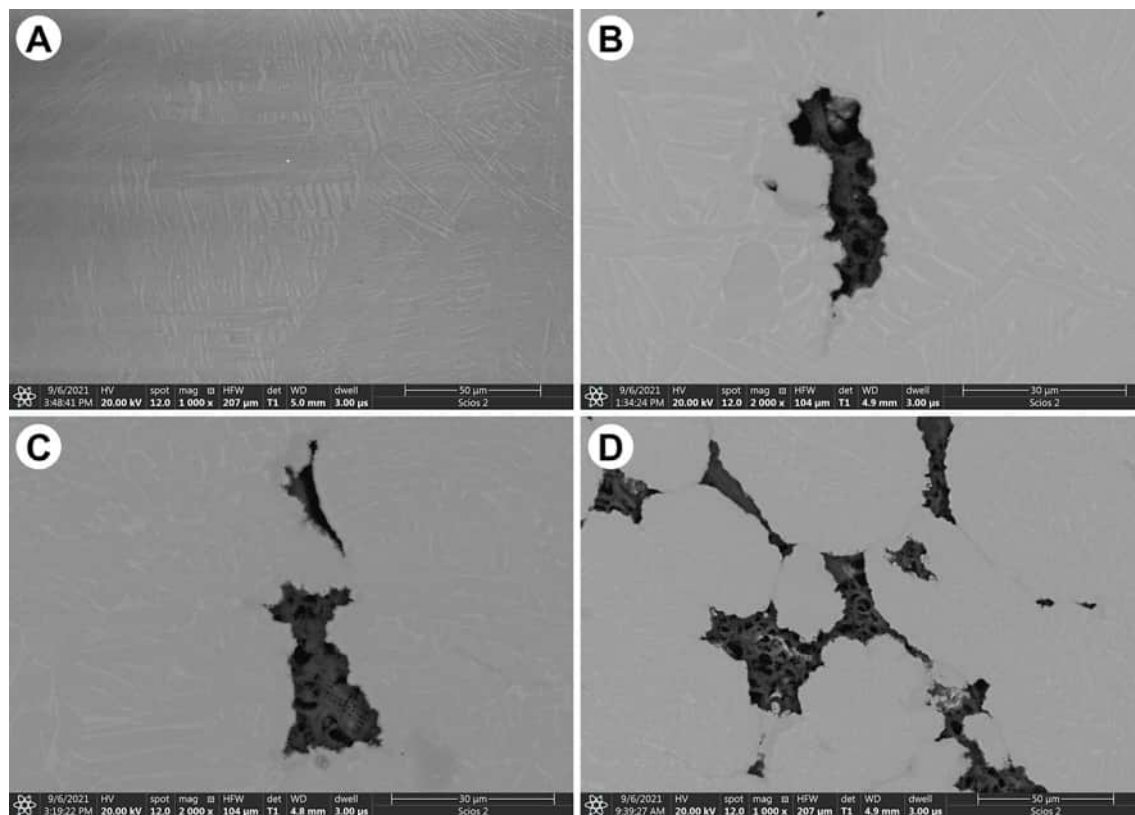


**Figure 2.** SEM images in the BSE mode of composite: (a) Ti6Al4V alloy, (b) Ti6Al4V/1% DE, (c) Ti6Al4V/5% DE, (d) Ti6Al4V/10% DE.

which is below the resolution limit of SEM observations performed. The higher than theoretical values of density for composite samples might be related to changes in the structure/morphology of DE under the consolidation conditions.

**Scanning electron microscopy observations.** SEM images of diatomaceous earth-reinforced Ti6Al4V alloys are shown in Fig. 2. The backscatter mode reveals in the metallic matrix two phase lamellar structure, which is characteristic for the Ti6Al4V alloy<sup>7,46</sup>. The SEM image of the sample without addition of DE (Fig. 2A) proves good consolidation, with no pores detected—see also results of density measurements. It has been noted that the addition of DE ceramic particles results in a reduction of the size of grains in the metallic matrix, which is in good agreement with<sup>7</sup>. SEM examinations revealed that DE-rich particles are characterized by a highly developed surface and irregular shapes. This indicates relatively poor wetting of DE by the metallic matrix. The DE particles are located in between the grains of the Ti6Al4V—Fig. 2B, filling out the space available during sintering. Taking into account size of individual frustules and size of DE particles in the composites with linear dimensions, c.a. 30  $\mu\text{m}$ , one can conclude that the particles are agglomerates of the frustules.

The SEM image of the fracture surface of the Ti6Al4V alloy (Fig. 3A) shows the presence of many ductile dimples and ductile tearing ridges, which suggest a ductile mode of failure. Fracture surface topography of the composites indicates that DE addition reduces ductility.

Good bonding between matrix and filler can be inferred from SEM images, e.g., Fig. 3, Figure S2—Figure S4. In-prints of frustules are clearly seen and intact frustules can be found in composite samples (white arrows, Fig. 3; see also Figure S2—Figure S4 in Supplementary Information). The SEM images revealed that diatom frustules are empty inside and can be treated as a “caged pores”, see Figs. 2, 3.

**X-ray diffraction analysis.** Obtained XRD diagrams are shown in Fig. 4. It can be noted that no peak is observed of a V compound. This indicates that V is in solid solution. Oxygen has been found in TiAl<sub>2</sub>O<sub>5</sub> (ICSD no. 98-015-4474) that exhibits hexagonal type structure (P 63/mmc no. 194). Addition of DE results in the shift to the right of the Bragg peaks. This might be an indication of residual strains generated in the composite matrix. Such strains are expected due to the mismatch in the coefficients of thermal expansion of Ti-rich matrix and DE particles. It can be noted that with the increasing volume fraction of DE, some diffraction peaks of Ti are reduced significantly because of the rising residual stresses and decreased fraction of a crystalline phase (Ti-rich) phase.

**Contact angle analyses.** The results of the investigations of surface wettability via measurements of the contact angle for sintered Ti6Al4V alloys with and without diatomaceous earth as a reinforcement are presented in Table 1 and Figure S5 (see Supplementary Information). The addition of the DE causes insignificant changes in

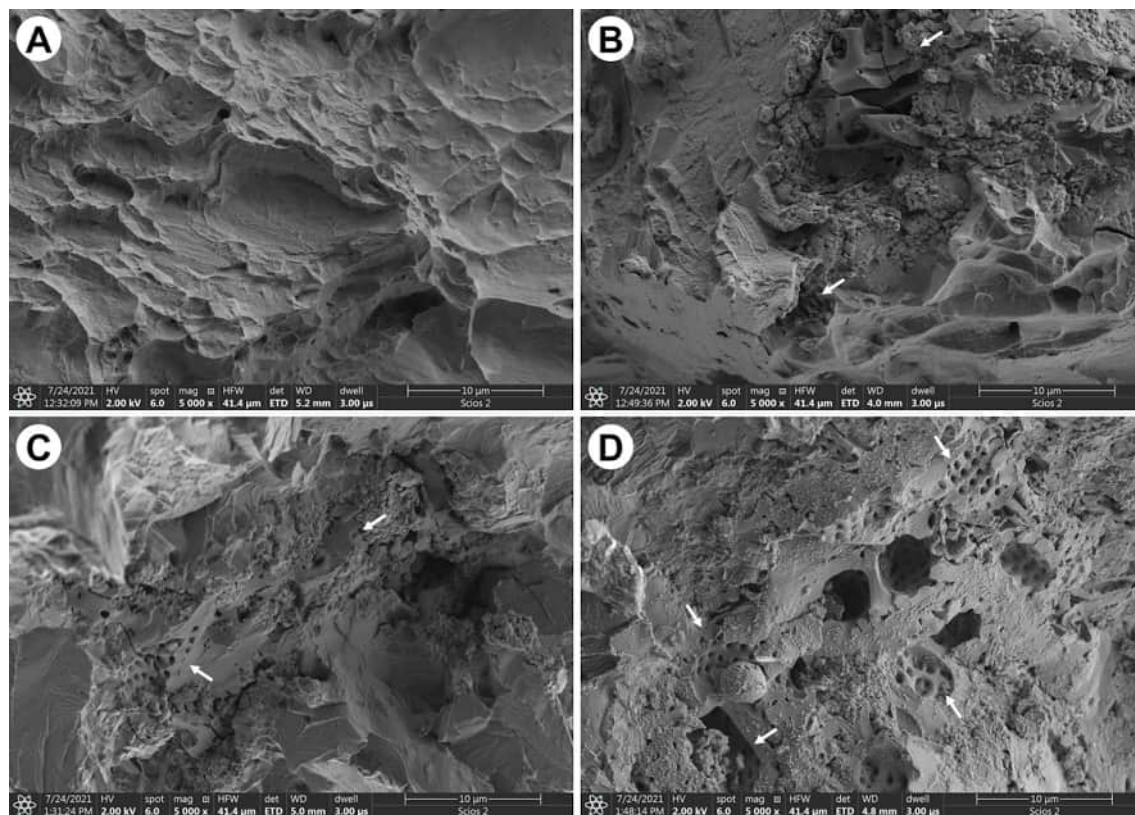


**Figure 3.** SEM images of fracture surfaces in the composite specimens: (a) Ti6Al4V alloy, (b) Ti6Al4V/1%DE, (c) Ti6Al4V/5% DE, (d) Ti6Al4V/10% DE; white arrows—in-prints of diatom frustules in the metallic matrix.

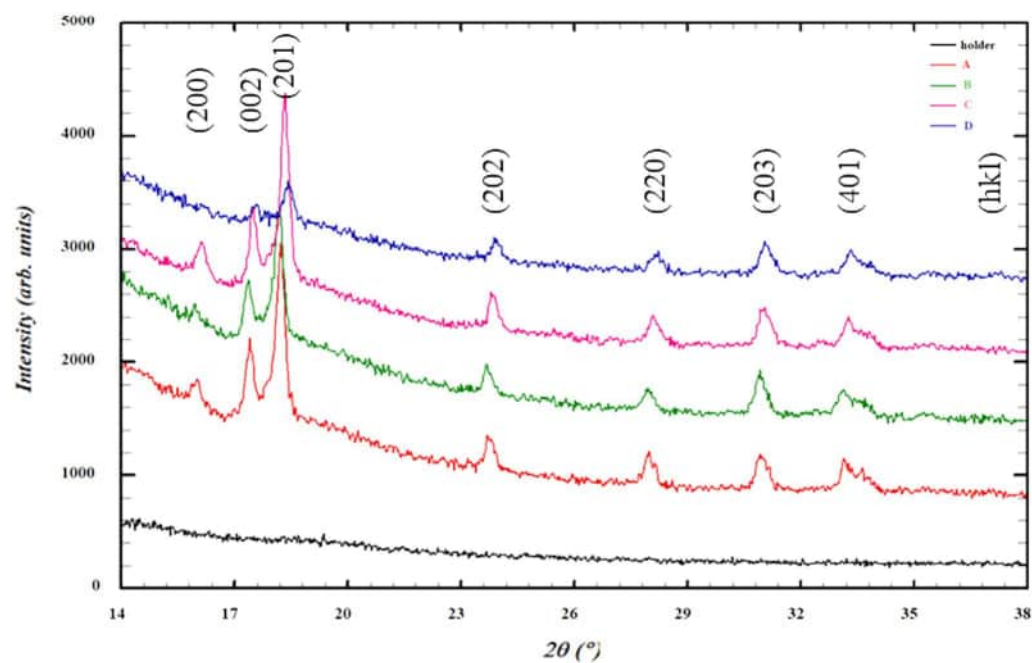


**Figure 4.** X-ray diffractograms of the sintered Ti6Al4V alloy composites with and without biogenic filler. Series: A—0%, B—1%, C—5%, D—10%.

Series	Wetting angle [°]
A	54.56 ± 1.29
B	55.54 ± 2.35
C	57.06 ± 1.58
D	57.66 ± 2.28

**Table 1.** The average values with a standard deviation of the contact angle of the sintered Ti6Al4V alloy composites with and without biogenic filler. Series: A—0%, B—1%, C—5%, D—10%.

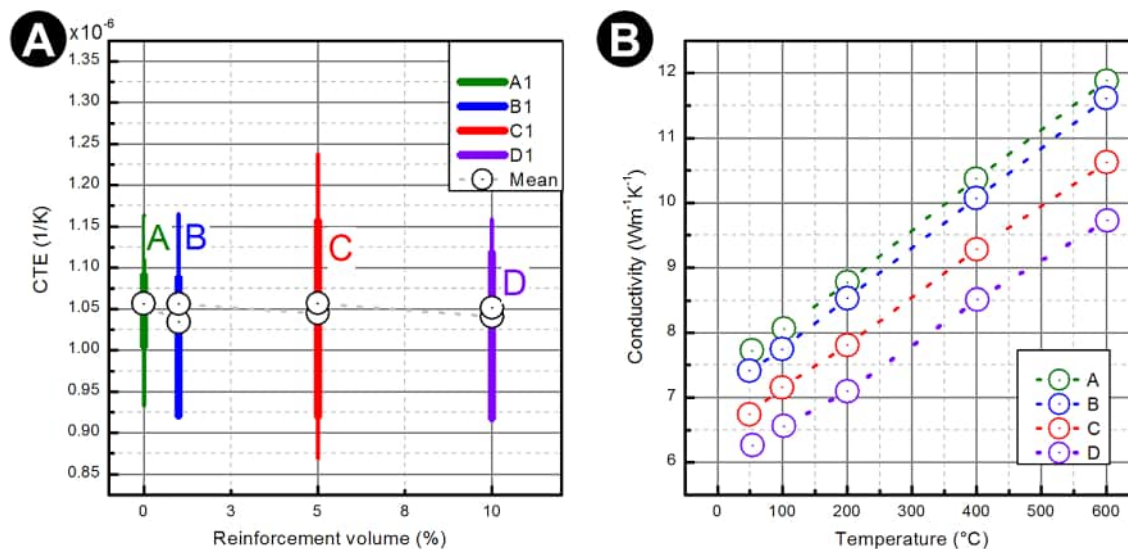


**Figure 5.** (A) The coefficient of the thermal expansion of the sintered Ti5Al4V alloy composites with and without biogenic filler. (B) The thermal conductivity as a function of temperature for sintered Ti6Al4V alloy composite with and without biogenic filler. Series: A—0%, B—1%, C—5%, D—10%.

the contact angle towards reducing hydrophilicity (from 54.56 for the pure alloy to 57.66 for 10% of reinforcement).

**Thermo-mechanical properties.** The coefficient of thermal expansion (CTE) and thermal conductivity ( $\lambda$ ) were obtained for the manufactured sample. Results are presented in Fig. 5A.

The importance of the coefficient of thermal expansion (CTE) of investigated samples is strictly related to the thermal properties of the material that affect the generation of tensile residual stresses. The coefficient of thermal expansion of ceramic reinforcement, regardless of its form, is smaller than that of most metallic matrices. Because of that lower coefficient, the thermal stresses, when the composite is subjected to temperature change, will be generated in both components—matrix and reinforcement. The predicted thermal properties are hard to realize due to the structure of the composites, interface as well as plastic deformation of the matrix due to internal thermal stresses.

The results show that the addition of the ceramic filler in the form of the diatomaceous earth does not cause major changes in mean apparent values of CTE for the composite specimens. On the other hand, CTE values for manufactured MMCs are characterized by a significantly higher dispersion of the measured values in comparison to a pure Ti6Al4V alloy.

The graphic depiction of the thermal conductivity (Fig. 5B) clearly shows an increase in conductivity with the temperature. The addition of the ceramic reinforcement results in lowering the conductivity, which is in good agreement with theory.

**Mechanical properties.** The effect of the various volume fractions of the ceramic filler on micro-hardness is presented in Fig. 6 and in Table 2. It is observed that reinforcement of Ti6Al4V with diatomaceous earth increases the microhardness, from 314.96 HV, up to 378.37 HV and 512.29 HV, for 5 and 10% DE, respectively. It should be noted that an addition of 1% reinforcement results in significantly increase (20%) of hardness.

Hayat et al. (2019) reported that the incorporation of hard ceramic particles in ductile titanium matrix significantly enhance its hardness<sup>10</sup>. Based on the graphical representation of the results obtained herein, departure from the rule of mixing is observed in the current case, indicating overlapping of strengthening and softening effects of DE reinforcement.

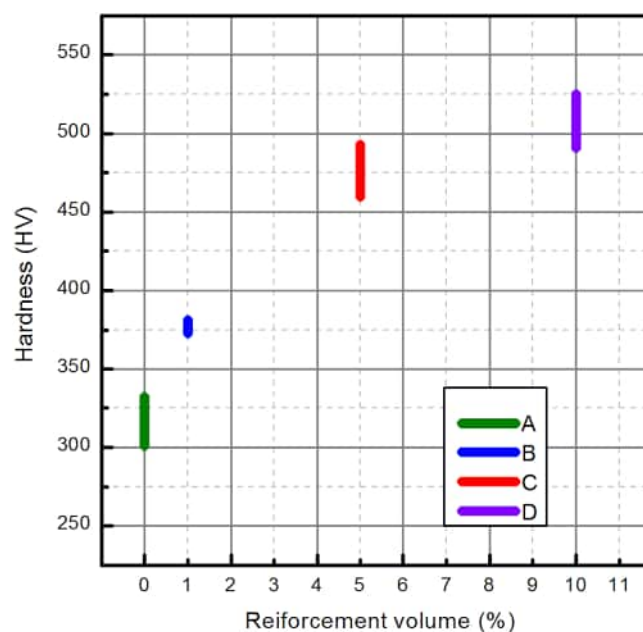


**Figure 6.** Hardness of Ti6Al4V based composites plotted against the content of the ceramic reinforcement.

Series	HV5
A	314.96 ± 13.07
B	378.37 ± 3.33
C	476.79 ± 13.35
D	512.29 ± 13.80

**Table 2.** Results of the hardness measurements via Vickers method. Series: A—0%, B—1%, C—5%, D—10%.

Series	R <sub>0.2t</sub> [MPa]	R <sub>mt</sub> [MPa]	A <sub>t</sub> [%]
A	767 ± 20	871 ± 11	9.00 ± 1.20
B	968 ± 35	1038 ± 12	1.34 ± 0.13
C	–	522 ± 75	0.08 ± 0.02
D	–	187 ± 24	0.03 ± 0.01

**Table 3.** Results of the static tensile test. Series: A—0%, B—1%, C—5%, D—10% content of the ceramic reinforcement.

Results of the tensile test are presented in Table 3 and Fig. 7A. Compared to pure Ti6Al4V, TMC with 1% diatomaceous earth demonstrated higher strength parameters (both yield strength R<sub>0.2t</sub> and tensile strength R<sub>mt</sub>). On the other hand, for 5 and 10 vol% of reinforcement, a decrease in tensile strength was observed. In fact specimens, with these volume fractions of DE, (5 and 10%) fractured below reaching a yield strength, exhibiting properties typical of ceramics. This is a clear indication that above 5% of volume fraction of DE, DE particles act as stress concentrators causing fracture prior to reaching yield point.

Fracture surface SEM images are presented in Supplementary Information (see Figure S6). The fracture surface of pure Ti6Al4V alloy shows various sizes of dimples. The addition of the reinforcement in the form of diatomaceous earth results in a mixture of brittle and ductile areas. The planar facets reveal in-prints caused by detachment of frustules present in DE.

Figure 7B shows the compressive stress–strain curves of the spark plasma sintered samples, whereas the values are presented in Table 4. The stress–strain curves show typical elastic–plastic deformation. An increase in the amount of the filler (1% and 5%) results in an increase in compression strength. The highest compression stress of 2159 MPa was obtained for the specimens with 5% of filler.

The result of the tests of mechanical properties of specimens can be discussed in terms: (a) effect of DE addition on the properties of Ti–rich matrix and (b) reaction of the composite structures to the applied load

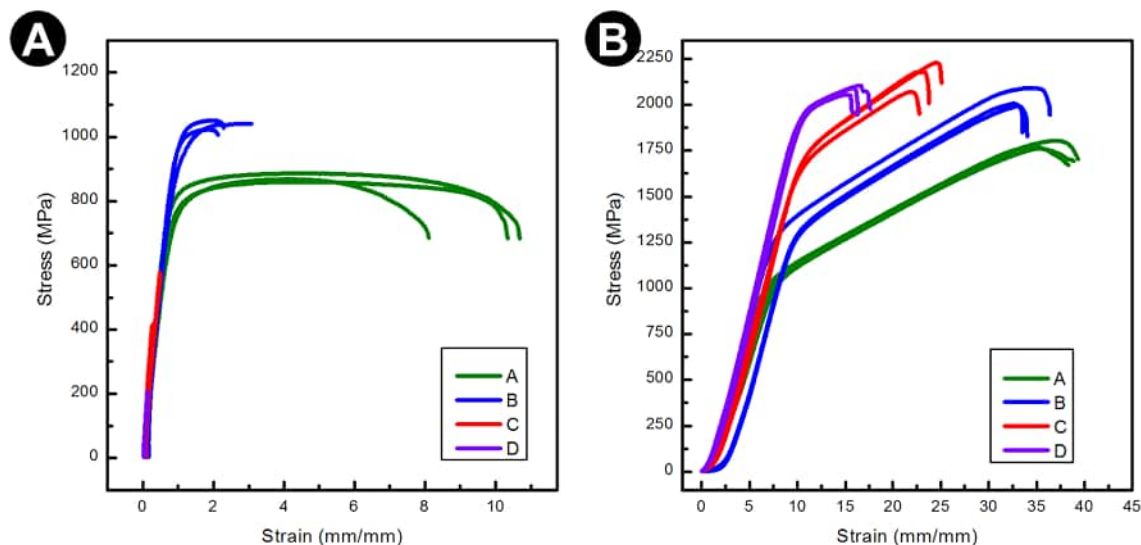


**Figure 7.** Stress–strain curve of manufactured composites Ti6Al4V/DE from the (A) tensile test, (B) static compression test. Series: A—0%, B—1%, C—5%, D—10% content of the ceramic reinforcement.

Series	$R_{2c}$ [MPa]	$R_{mc}$ [MPa]	$A_c$ [%]
A	$1111 \pm 9$	$1778 \pm 18$	$38.9 \pm 0.40$
B	$1384 \pm 7$	$2030 \pm 44$	$34.6 \pm 1.30$
C	$1801 \pm 27$	$2159 \pm 66$	$23.9 \pm 0.90$
D	$2009 \pm 7$	$2083 \pm 21$	$16.6 \pm 0.80$

**Table 4.** Results of the static compression test. Series: A—0%, B—1%, C—5%, D—10% content of the ceramic reinforcement.

in tensile/compression. With regard to the effect of DE addition on the metallic matrix, it can be noted that composite samples are characterized by a smaller grain size of Ti crystals, which brings about a higher value of the yield flow of the composite matrix. The mechanism responsible for the size of grains in the Ti-rich matrix is very likely blocking of grain growth during sintering by DE particles. In fact, microstructures shown in Fig. 2 clearly show that DE particles are located in boundaries of Ti crystals. In addition to grain size refinement on the strengthening of Ti-matrix, one should also take into account the effect of geometrically-necessary dislocations needed to accommodate differences in the thermal contraction of the Ti-matrix and DE particles upon cooling from sintering temperature. In summary, presence of DE strengthens metal matrix in the composites of interest. On the other hand, DE particles have much lower mechanical strength than the Ti matrix and their presence reduces effective load bearing cross-sections of the specimens and thus brings about a reduction of composite strength. DE particles act also as stress concentrators, promoting brittle fracture of specimens in tensile tests. Thus, depending on the mode of applied load (tensile, compression, Vickers hardness) mechanical properties of the composite are determined by interplay between strengthening and weakening impact of DE particles. Strengthening effects dominate for small volume fractions and for compression mode. Recognition of these dichotomies on the impact of DE particles allows for selecting their appropriate volume fractions to given applications of the composites in question.

## Conclusions

The novel composites Ti6Al4V/diatomaceous earth have been fabricated using the spark plasma sintering (SPS) method. SEM images of these composites revealed that this technological route preserved the diatoms. The matrix does not penetrate the reinforcement, and good bonding between matrix and biogenic filler has been obtained. The increase of DE content within composites results in a decrease of the hydrophilicity—towards hydrophobicity.

The XRD measurements allowed us to identify the TiAl<sub>2</sub>O<sub>5</sub> phase. No silicide phase was found. XRD spectra also revealed residual stresses generated by particles of DE.

Compared with samples sintered without filler, with the increase of DE content, the compressive yield strength increased while the plasticity gradually decreased. Especially for Ti6Al4V-5 vol% DE composite, the compressive yield strength is 1801 MPa, which is ca. 62% higher than that of pure Ti6Al4V (1111 MPa). Additionally, it maintains good compressive plasticity (34.6%). In the case of the tensile test, the highest values have been obtained for Ti6Al4V-1 vol% DE composite, for which the tensile yield strength was 968 MPa, which is ca. 26% higher than that of pure titanium (767 MPa) and maintain acceptable tensile strain.

In the case of the mean values of the coefficient of thermal expansion (CTE), no significant differences for pure Ti6Al4V alloy and with the addition of ceramic filler (DE) have been noticed. The thermal conductivity has been lowered with the addition of diatomaceous earth.

Comparison of our results with the values presented in the literature clearly show that the samples with 1 vol% and 5 vol% DE demonstrated better tensile strength than elements sintered by the BE method. At the same time compression strength exceeds 2000 MPa. This is remarkably high value making the composites fabricated here a promising candidate for manufacturing of devices in which applied loads primarily generate compressive stresses.

The results show that biogenic filler in the form of diatom frustules can be used as an attractive reinforcement for future applications in development of high-performance TMCs, e.g., for aerospace, automotive, and sporting goods.

## Experimental

**Materials.** Ti6Al4V (UNS R56400/3.7165), Titanium Grade 5, spherical powder (Wolften, Wroclaw, Poland) with a particle size: 0–53  $\mu\text{m}$  (density 2.53  $\text{g}/\text{cm}^3$ ) and 53–105  $\mu\text{m}$  (density 2.56  $\text{g}/\text{cm}^3$ ) was used. Diatomaceous earth (DE, Diatomite, Perma-Guard) consisting of shells of unicellular microscopic organisms (*Aulacoseira* sp.) from the extremely clean freshwater deposits was used as a filler.

**Manufacturing of composites.** Mixtures of Ti6Al4V and diatomaceous earth (DE) were used in the experimental part. The SPS process was conducted under vacuum at the uniaxial compressive pressure of 1.2 MPa. The powder mixtures were placed in cylindrical graphite dies with an inner diameter of 25 mm and pressed between two graphite punches. The mixtures were heated up to 1000  $^\circ\text{C}$  with a heating rate of 50  $^\circ\text{C} \times \text{min}^{-1}$  and maintained at final temperature for 5 min. The process has been conducted in inert gas—Argon at  $-0.5$  Atm pressure. The relative density of the samples, determined by the Archimedes method, was estimated at 100% of the theoretical value.

**Experimental techniques.** *Characterization of powders and consolidated samples.* Characterization of Ti6Al4V powder and diatomaceous earth DIATOMIT (Perma-Guard, USA) was carried out using an ultra-high-resolution analytical dual-beam FIB-SEM tool (Scios2 DualBeam, Thermo Fisher Scientific, Waltham, MA, USA). Powder samples were coated with Au (5 nm layer) using a high-vacuum sputter coater. Elemental analyses of Ti6Al4V powders and diatomaceous earth were carried out using Energy Dispersive X-ray Spectroscopy (EDS). Elemental maps were collected under an acceleration voltage of 30 kV, elemental range of 10 keV.

The grain size distribution of the Ti6Al4V powder was measured by a Laser Particle Size Analyzer (Fritsch, Idar-Oberstein, Germany) in water suspension. The distribution of the size of diatom frustules was measured using Air Jet Sieving Machine AS200 jet (Retsch, Germany) during the fractionation process.

The experimental density (bulk density) of the composites was obtained by the Archimedes method. The theoretical density was calculated using the rule of mixture. Bulk density was calculated by using Eq. (1):

$$\rho_B = \frac{m_d}{m_{\text{sat}} - m_{\text{sus}}} \cdot \rho_{\text{H}_2\text{O}} \quad (1)$$

where  $\rho_B$ —the bulk density,  $m_{\text{sat}}$ —saturated mass,  $m_d$ —dry mass,  $m_{\text{sus}}$ —suspended immersion mass.

X-ray diffraction (XRD) measurements at room temperature were performed using an Empyrean Panalytical powder diffractometer equipped with Mo X-ray tube ( $K_\alpha$  radiation,  $\lambda = 0.7093187$  Å, 40 kV, 40 mA) and PixCell1D strip detector. The scattered intensity was recorded in the Bragg–Brentano geometry in a range of  $2\theta$  from  $14^\circ$  to  $38^\circ$  in steps of  $0.026261^\circ$ . The pattern acquisitions have been conducted on solid samples ( $4 \times 4$  mm) on a plexiglass holder. The small area ( $4 \times 4$  mm) of solid samples required a narrow fixed slit. The change of the aperture led to the much smaller response from the background (plexiglass cover) in the diffractogram. The phase analysis was carried out based on the ICSD database using the HighScore program<sup>47</sup>.

Contact angle measurements were performed by the sessile drop technique at room temperature and atmospheric pressure, with a Osilla Contact Angle Goniometer (Osilla, Sheffield, UK). Ten independent measurements were performed for each sample, each with a 2  $\mu\text{l}$  water drop. In order to examine the macroscopic characteristic and to eliminate the effect of topography, the measurements of contact angle have been conducted on the polished cross-sections. The obtained results were averaged to reduce the impact of surface nonuniformity.

The hardness of the composite samples was tested by the Vickers method using a Hardness Tester DuraScan 20 (Struers) with the load HV5 (ca. 49.03 N) according to the PN-EN ISO 6507-1.

The coefficient of thermal expansion, CTE, was measured using the standard four-probe method in a vacuum. The thermal conductivity,  $\lambda$ , was calculated according to the formula  $\lambda = \alpha \cdot C_p \cdot \rho$ , where  $C_p$  is the theoretical heat capacity based on the measurements via laser flash method (LFA, Netzsch, 457 MicroFlash) using a sample with a diameter of 10 mm and height of 1 mm. All measurements were performed over the temperature range of 323 K to 723 K.

The static tensile tests were carried out using the Small-Specimen Tensile Test (SSTT) technique<sup>48–50</sup>. Samples with the dimensions given in Supplementary Information (see Figure S1) were tested with a Zwick/Roell Z005 (ZwickRoell GmbH & Co. KG, Germany) universal electromechanical testing machine equipped with a load cell having a load capacity of  $\pm 1$  kN. The tests were controlled by a crosshead displacement of the testing machine of 0.005 mm/s. The initial strain rate was  $1 \times 10^{-1}$  1/s.

Because of the small size of the testing specimens, a non-contact optical method based on image correlation was applied (DIC-Digital Images Correlation) for strain calculations. Local deformations, and the fields of deformations over the entire area of a tested specimen, were analyzed using VIC 2d commercial software provided by Correlated Solutions Inc. The values of the engineering stress–strain curves were calculated by

post-processing DIC analysis. For the static compression tests, cube specimens with a characteristic dimension of 3 mm were used. The test was controlled by constant displacement in time (0,003 mm/s), and the strain rate was finally the same as in tensile  $1 \times 10^{-1}$  1/s. For the compression tests, non-standard yield strength at 2% of the plastic strain was calculated.

### Data availability

All data generated or analysed during this study are included in this published article (and its Supplementary Information files).

Received: 3 March 2022; Accepted: 16 May 2022

Published online: 24 May 2022

### References

- Evans, A., San Marchi, C. & Mortensen, A. *Metal Matrix Composites in Industry* (Springer, 2003). <https://doi.org/10.1007/978-1-4615-0405-4>.
- Rosso, M. Ceramic and metal matrix composites: Routes and properties. *J. Mater. Process. Technol.* **175**, 364–375 (2006).
- Morsi, K. & Patel, V. V. Processing and properties of titanium–titanium boride (TiBw) matrix composites—a review. *J. Mater. Sci.* **42**, 2037–2047 (2007).
- Geng, L., Ni, D. R., Zhang, J. & Zheng, Z. Z. Hybrid effect of TiBw and TiCp on tensile properties of in situ titanium matrix composites. *J. Alloys Compd.* **463**, 488–492 (2008).
- Munir, K. S., Kingshott, P. & Wen, C. Carbon nanotube reinforced titanium metal matrix composites prepared by powder metallurgy—A review. *Crit. Rev. Solid State Mater. Sci.* **40**, 38–55 (2015).
- Shivakumar, N., Vasu, V., Narasaiah, N. & Kumar, S. Synthesis and characterization of nano-sized Al<sub>2</sub>O<sub>3</sub> particle reinforced ZA-27 metal matrix composites. *Proc. Mater. Sci.* **10**, 159–167 (2015).
- Sivakumar, G., Ananthi, V. & Ramanathan, S. Production and mechanical properties of nano SiC particle reinforced Ti–6Al–4V matrix composite. *Trans. Nonferrous Met. Soc. China* **27**, 82–90 (2017).
- Kumar, P. & Chandran, K. S. R. Strength–ductility property maps of powder metallurgy (PM) Ti–6Al–4V alloy: A critical review of processing–structure–property relationships. *Metall. Mater. Trans. A* **48**, 2301–2319 (2017).
- Konstantinov, A. S., Bazhin, P. M., Stolin, A. M., Kostitsyna, E. V. & Ignatov, A. S. Ti–B-based composite materials: Properties, basic fabrication methods, and fields of application (review). *Compos. Part A Appl. Sci. Manuf.* **108**, 79–88 (2018).
- Hayat, M. D., Singh, H., He, Z. & Cao, P. Titanium metal matrix composites: An overview. *Compos. Part A Appl. Sci. Manuf.* **121**, 418–438 (2019).
- Kondoh, K. Titanium metal matrix composites by powder metallurgy (PM) routes. In *Titanium Powder Metallurgy 277–297* (Elsevier, 2015). <https://doi.org/10.1016/B978-0-12-800054-0.00016-2>.
- Fang, Z. Z. *et al.* Powder metallurgy of titanium—past, present, and future. *Int. Mater. Rev.* **63**, 407–459 (2018).
- Eylon, D. & Pierce, C. M. Effect of microstructure on notch fatigue properties of Ti–6Al–4V. *Metall. Trans. A* **7**, 111–121 (1976).
- Yoder, G. R., Cooley, L. A. & Crooker, T. W. Observations on microstructurally sensitive fatigue crack growth in a widmanstätten Ti–6Al–4V alloy. *Metall. Trans. A* **8**, 1737–1743 (1977).
- Margolin, H. & Mahajan, Y. Void formation, void growth and tensile fracture in Ti–6Al–4V. *Metall. Trans. A* **9**, 781–791 (1978).
- Materials Properties Handbook. *Titanium Alloys* (ASM International, 1993).
- Froes, F. H. & Eylon, D. Powder metallurgy of titanium alloys. *Int. Mater. Rev.* **35**, 162–184 (1990).
- Hagiwara, M., Kaieda, Y., Kawabe, Y. & Miura, S. Fatigue property enhancement of .ALPHA.-.BETA. Titanium alloys by blended elemental P/M approach. *ISIJ Int.* **31**, 922–930 (1991).
- Fujita, T., Ogawa, A., Ouchi, C. & Tajima, H. Microstructure and properties of titanium alloy produced in the newly developed blended elemental powder metallurgy process. *Mater. Sci. Eng. A* **213**, 148–153 (1996).
- Haase, C., Lapovok, R., Ng, H. P. & Estrin, Y. Production of Ti–6Al–4V billet through compaction of blended elemental powders by equal-channel angular pressing. *Mater. Sci. Eng. A* **550**, 263–272 (2012).
- Abouelmagd, G., Büchkremer, H. P., El-Magd, E. & Stöver, D. Mechanical properties of a TiAl6V4 alloy processed by powder metallurgy. *J. Mater. Process. Technol.* **37**, 583–597 (1993).
- Zhang, K., Mei, J., Wain, N. & Wu, X. Effect of hot-isostatic-pressing parameters on the microstructure and properties of powder Ti–6Al–4V hot-isostatically-pressed samples. *Metall. Mater. Trans. A* **41**, 1033–1045 (2010).
- Xu, L., Guo, R., Bai, C., Lei, J. & Yang, R. Effect of hot isostatic pressing conditions and cooling rate on microstructure and properties of Ti–6Al–4V alloy from atomized powder. *J. Mater. Sci. Technol.* **30**, 1289–1295 (2014).
- Kim, Y., Kim, E.-P., Song, Y.-B., Lee, S. H. & Kwon, Y.-S. Microstructure and mechanical properties of hot isostatically pressed Ti–6Al–4V alloy. *J. Alloys Compd.* **603**, 207–212 (2014).
- Bozic, D., Sekulic, D., Stasic, J., Rajkovic, V. & Jovanovic, M. T. The influence of microstructural characteristics and contaminants on the mechanical properties and fracture topography of low cost Ti6Al4V alloy. *Int. J. Mater. Res.* **99**, 1268–1274 (2008).
- Azevedo, C. R. F. & Flower, H. M. Calculated ternary diagram of Ti–Al–Si system. *Mater. Sci. Technol.* **16**, 372–381 (2000).
- Azevedo, C. R. F. & Flower, H. M. Experimental and calculated Ti-rich corner of the Al–Si–Ti ternary phase diagram. *Calphad* **26**, 353–373 (2002).
- Pauffer, P. J. H. Westbrook, R. L. Fleischer (eds.). *Intermetallic Compounds. Principles and Practice*. John Wiley & Sons, Chichester 1995. Vol. 1. Principles. 1126 S. ISBN 0–471–94219–7. Vol. 2. Practice. 752 S. ISBN 0–471–93454–2. Set: ISBN 0–471–93453–4. Preis: *Cryst. Res. Technol.* **30**, 920–920 (1995).
- Anpo, M. *et al.* Photoluminescence and photocatalytic activity of highly dispersed titanium oxide anchored onto porous Vycor glass. *J. Phys. Chem.* **89**, 5017–5021 (1985).
- Fu, X., Clark, L. A., Yang, Q. & Anderson, M. A. Enhanced photocatalytic performance of titania-based binary metal oxides: TiO<sub>2</sub>/SiO<sub>2</sub> and TiO<sub>2</sub>/ZrO<sub>2</sub>. *Environ. Sci. Technol.* **30**, 647–653 (1996).
- Gao, X. & Wachs, I. E. Titania–silica as catalysts: molecular structural characteristics and physico-chemical properties. *Catal. Today* **51**, 233–254 (1999).
- Guo, X.-C. & Dong, P. Multistep coating of thick titania layers on monodisperse silica nanospheres. *Langmuir* **15**, 5535–5540 (1999).
- Mogyorósi, K., Dékány, I. & Fendler, J. H. Preparation and characterization of clay mineral intercalated titanium dioxide nanoparticles. *Langmuir* **19**, 2938–2946 (2003).
- Hirano, M. & Ota, K. Direct formation and photocatalytic performance of anatase (TiO<sub>2</sub>)/Silica (SiO<sub>2</sub>) composite nanoparticles. *J. Am. Ceram. Soc.* **87**, 1567–1570 (2004).
- Lee, J.-W., Kong, S., Kim, W.-S. & Kim, J. Preparation and characterization of SiO<sub>2</sub>/TiO<sub>2</sub> core-shell particles with controlled shell thickness. *Mater. Chem. Phys.* **106**, 39–44 (2007).

36. Kibanova, D., Trejo, M., Destailats, H. & Cervinisilva, J. Synthesis of hectorite–TiO<sub>2</sub> and kaolinite–TiO<sub>2</sub> nanocomposites with photocatalytic activity for the degradation of model air pollutants. *Appl. Clay Sci.* **42**, 563–568 (2009).
37. Sharma, N. *et al.* Diatoms biotechnology: Various industrial applications for a greener tomorrow. *Front. Mar. Sci.* **8**, 2 (2021).
38. Eriksson, M., Shen, Z. & Nygren, M. Fast densification and deformation of titanium powder. *Powder Metall.* **48**, 231–236 (2005).
39. Orrù, R., Licheri, R., Locci, A. M., Cincotti, A. & Cao, G. Consolidation/synthesis of materials by electric current activated/assisted sintering. *Mater. Sci. Eng. R Rep.* **63**, 127–287 (2009).
40. Ertorer, O., Topping, T. D., Li, Y., Moss, W. & Lavernia, E. J. Nanostructured Ti consolidated via spark plasma sintering. *Metall. Mater. Trans. A* **42**, 964–973 (2011).
41. Despang, F. *et al.* Response of human bone marrow stromal cells to a novel ultra-fine-grained and dispersion-strengthened titanium-based material. *Acta Biomater.* **6**, 1006–1013 (2010).
42. Quan, Y. *et al.* Ti6Al4V foams fabricated by spark plasma sintering with post-heat treatment. *Mater. Sci. Eng. A* **565**, 118–125 (2013).
43. Zhang, F., Reich, M., Kessler, O. & Burkel, E. The potential of rapid cooling spark plasma sintering for metallic materials. *Mater. Today* **16**, 192–197 (2013).
44. Ghesmati Tabrizi, S., Sajjadi, S. A., Babakhani, A. & Lu, W. Influence of spark plasma sintering and subsequent hot rolling on microstructure and flexural behavior of in-situ TiB and TiC reinforced Ti6Al4V composite. *Mater. Sci. Eng. A* **624**, 271–278 (2015).
45. Hao, Y. *et al.* Rapid preparation of TiC reinforced Ti6Al4V based composites by carburizing method through spark plasma sintering technique. *Mater. Des.* **65**, 94–97 (2015).
46. Jovanović, M. T., Tadić, S., Zec, S., Mišković, Z. & Bobić, I. The effect of annealing temperatures and cooling rates on microstructure and mechanical properties of investment cast Ti–6Al–4V alloy. *Mater. Des.* **27**, 192–199 (2006).
47. Degen, T., Sadki, M., Bron, E., König, U. & Nénert, G. The HighScore suite. *Powder Diff.* **29**, S13–S18 (2014).
48. Molak, R. M. *et al.* Use of micro tensile test samples in determining the remnant life of pressure vessel steels. *Appl. Mech. Mater.* **7–8**, 2 (2007).
49. Molak, R. M. *et al.* Measurement of mechanical properties in a 316L stainless steel welded joint. *Int. J. Press. Vessel. Pip.* **86**, 2 (2009).
50. Molak, R. M., Kartal, M. E., Pakielna, Z. & Kurzydowski, K. J. The effect of specimen size and surface conditions on the local mechanical properties of 14MoV6 ferritic–pearlitic steel. *Mater. Sci. Eng. A* **651**, 2 (2016).

## Acknowledgements

Izabela Zgłobicka acknowledges the funding provided by National Science Center for providing financial support to project Metal Matrix Composites with natural filler (Grant No. 2018/31/D/ST8/00890). The X–ray diffraction analysis was supported by the National Science Centre under grant OPUS no. 2018/31/B/ST3/00279. The authors are grateful to Prof. John P. Kocielek from the University of Colorado Boulder for critically reading the manuscript and correcting the language.

## Author contributions

I.Z.: conceptualization, methodology, validation, formal analysis, investigation, resources, writing—original draft, writing—review & editing, visualization, supervision, project administration, funding acquisition; R.Z.: methodology, investigation, writing—review & editing; K.K.: methodology, investigation, visualization, writing—review & editing; R.M.: methodology, investigation, writing—review & editing; M.W.: investigation; K.R.: investigation, writing—review & editing; B.F.: investigation; K.J.K.: writing—review & editing, supervision.

## Competing interests

The authors declare no competing interests.

## Additional information

**Supplementary Information** The online version contains supplementary material available at <https://doi.org/10.1038/s41598-022-12855-5>.

**Correspondence** and requests for materials should be addressed to I.Z.

**Reprints and permissions information** is available at [www.nature.com/reprints](http://www.nature.com/reprints).

**Publisher's note** Springer Nature remains neutral with regard to jurisdictional claims in published maps and institutional affiliations.



**Open Access** This article is licensed under a Creative Commons Attribution 4.0 International License, which permits use, sharing, adaptation, distribution and reproduction in any medium or format, as long as you give appropriate credit to the original author(s) and the source, provide a link to the Creative Commons licence, and indicate if changes were made. The images or other third party material in this article are included in the article's Creative Commons licence, unless indicated otherwise in a credit line to the material. If material is not included in the article's Creative Commons licence and your intended use is not permitted by statutory regulation or exceeds the permitted use, you will need to obtain permission directly from the copyright holder. To view a copy of this licence, visit <http://creativecommons.org/licenses/by/4.0/>.

© The Author(s) 2022

## Article

# Poly(lactic acid) Matrix Reinforced with Diatomaceous Earth

Izabela Zglobicka <sup>1,\*</sup> , Magdalena Joka-Yildiz <sup>2</sup> , Rafal Molak <sup>1</sup> , Michal Kawalec <sup>1</sup>, Adrian Dubicki <sup>1</sup>, Jakub Wroblewski <sup>1</sup>, Kamil Dydek <sup>3</sup> , Anna Boczkowska <sup>3</sup>  and Krzysztof J. Kurzydowski <sup>1</sup>

<sup>1</sup> Faculty of Mechanical Engineering, Bialystok University of Technology, Wiejska 45C, 15-351 Bialystok, Poland

<sup>2</sup> Faculty of Civil Engineering and Environmental Sciences, Bialystok University of Technology, Wiejska 45E, 15-351 Bialystok, Poland

<sup>3</sup> Faculty of Materials Science and Engineering, Warsaw University of Technology, Woloska 141, 02-507 Warsaw, Poland

\* Correspondence: i.zglobicka@pb.edu.pl

**Abstract:** The poly(lactic acid) (PLA) biodegradable polymer, as well as natural, siliceous reinforcement in the form of diatomaceous earth, fit perfectly into the circular economy trend. In this study, various kinds of commercial PLA have been reinforced with diatomaceous earth (DE) to prepare biodegradable composites via the extrusion process. The structure of the manufactured composites as well as adhesion between the matrix and the filler were investigated using scanning electron microscopy (SEM). Differential scanning calorimetry (DSC) analyses were carried out to determine crystallinity of PLA matrix as function of DE additions. Additionally, the effect of the ceramic-based reinforcement on the mechanical properties (Young's modulus, elongation to failure, ultimate tensile strength) of PLA has been investigated. The results are discussed in terms of possible applications of PLA + DE composites.

**Keywords:** PLA composites; diatomaceous earth; extrusion; biodegradable composites



**Citation:** Zglobicka, I.; Joka-Yildiz, M.; Molak, R.; Kawalec, M.; Dubicki, A.; Wroblewski, J.; Dydek, K.; Boczkowska, A.; Kurzydowski, K.J. Poly(lactic acid) Matrix Reinforced with Diatomaceous Earth. *Materials* **2022**, *15*, 6210. <https://doi.org/10.3390/ma15186210>

Academic Editor: Mingchun Zhao

Received: 22 July 2022

Accepted: 5 September 2022

Published: 7 September 2022

**Publisher's Note:** MDPI stays neutral with regard to jurisdictional claims in published maps and institutional affiliations.



**Copyright:** © 2022 by the authors. Licensee MDPI, Basel, Switzerland. This article is an open access article distributed under the terms and conditions of the Creative Commons Attribution (CC BY) license (<https://creativecommons.org/licenses/by/4.0/>).

## 1. Introduction

The latest trends in the development and manufacturing of novel materials are strictly related to the idea of the circular economy because of the environmental concerns as well as finite petroleum resources [1]. This approach particularly applies to polymer-based materials and results in increasing interest in research and development (R and D) work focused on biodegradable polymers.

One of the most promising and during the last decade the most intensively investigated biodegradable polymer is poly(lactic acid) (PLA). An advantage of the PLA is its commercial availability and remarkable properties which shall be tuned-up to meet the needs of specific applications. Properties of PLA can be further enhanced by various reinforcements: fibers (e.g., flax, kenaf, glass fibers) as well as particles (e.g., talc, hydroxyapatite, calcium carbonate) [2]. In the context of circular economy, diatomaceous earth—naturally occurring and consisting of fossilized remains of diatoms—is a promising modifier of PLA. One characteristic feature of diatoms is their highly ornamented siliceous shells, called frustules, which are known to have excellent resistance to cracking [3,4]. Recent research results clearly show that diatoms may also impart useful functional properties to diatom-reinforced composite materials [5–7].

Composites of PLA modified by DE have been recently studied by Dobrosielska et al. [6]. They demonstrated that addition of diatomaceous earth results in an increase in the tensile strength. Highest mechanical strength has been observed for the composites with 1 wt% of reinforcement, which transforms to 5.5 vol%. Additionally, intact diatoms frustules, obtained by aqua-agriculture, have been used as PLA reinforcement by Li et al. [8]. They reported penetration of the siliceous frustules by polymeric matrix. The results obtained by X-ray diffraction and differential scanning calorimetry analysis revealed that this type

of reinforcement acts as a nucleating agent increasing crystallinity. Tensile tests showed enhanced strength and ductility of PLA reinforced by diatom frustules [8].

Generally, the effect of reinforcements depends on their adhesion to the matrix. Aguero et al. [9] investigated several coupling agents such as (3-glycidyloxypropyl) trimethoxysilane, epoxy styrene-acrylic oligomer and maleinized linseed oil [9]. Additions of these compatibilizers result in improvement of the elastic modulus and ductile properties of PLA-DE composites [9]. Gonzalez et al. [10] showed an increase in the ductility of PLA-DE composites by the addition of MLO. PLA-DE composites can be used as filaments in 3D printing [11].

According to Singh et al. [12], screw extrusion technology allows to obtain materials—filaments—for 3D printing. Such approach gives possibility to use variable composition, size and type of reinforcements as well as matrix. Three-dimensional printed materials, especially composite structures, can be applied in various fields such as: biomedical, aerospace, military, automobile [12].

In this paper, the effect of silica diatomaceous earth reinforcement on microstructure, melting point, crystallization, thermal degradation and mechanical properties of PLA and DE composites have been investigated. Various kinds of commercial PLA have been used to fabricate composites for eco-friendly applications as of biodegradable plastic products.

## 2. Materials and Methods

### 2.1. Materials

Ingeo™ (NatureWorks, Plymouth, MN, USA) Biopolymers, types of PLA-based materials: 2003D, 3001D, 3251D and 4043D (Nature Works) with a melt flow index (MFI), based on technical data sheets, equal to: 6, 22, 80 and 6, respectively, were used in this study. These Ingeo™ Biopolymers differ also in suggested processing methods and applications. PLA 2003D can be easily processed via conventional extrusion, whereas 3001D and 3251D are designed for injection molding. Overall, 4043D is well-suited for 3D printing using many different types of printers and for a broad range of printing applications.

Diatomaceous earth (DE, Diatomite, Perma-Guard) with unicellular microscopic organisms (*Aulacoseira* sp.) was used as filler. The single frustule is characterized by a regular, cylindrical shape with numerous openings on the surface. The PLAs and DE were dried at 40 °C under vacuum prior to undertaking fabrication steps.

### 2.2. Fabrication of Composites

The mixtures of PLA and diatomaceous earth (DE) reinforcement (5%, 10% and 15% weight) have been repeatedly pressed using the hydraulic press Fontijne Presses LabEcon300 (Delft, The Netherlands). Each composite has been pressed at least 10 times at a temperature of 190 °C. Afterwards, prepared samples have been manually curated in form of flakes. Reference samples made of PLA only were prepared analogously.

The flakes were used to manufacture the filaments using the laboratory twin-screw extruder HAAKE MiniLab (ThermoFisher Scientific, Waltham, MA, USA). The process has been conducted at a constant temperature of 175 °C and 50 rpm.

The specific sample information is listed in Table 1.

### 2.3. Experimental Techniques

Observations of the morphology of the DE and its dispersion within the PLA composites were carried out using an ultra-high-resolution analytical dual-beam FIB-SEM tool (Scios2, DualBeam, ThermoFisher, Scientific, Waltham, MA, USA) under acceleration voltage of 2 kV. Observations were carried out at magnifications in the range of 500–5000×. For imaging at the highest resolution, samples were coated with a conductive (ca. 7 nm) layer of Cu/Ni using Precision Etching Coating System Model 682 (Gatan, Pleasanton, CA, USA). Observation was carried out of filaments fractured after cooling to the temperature of liquid nitrogen.

**Table 1.** The codes and composition of the prepared composite materials.

Sample	PLA (wt%)	DE (wt%)
2003-0	100	0
2003-5	95	5
2003-10	90	10
2003-15	85	15
3001-0	100	0
3001-5	95	5
3001-10	90	10
3001-15	85	15
3251-0	100	0
3251-5	95	5
3251-10	90	10
3251-15	85	15
4043-0	100	0
4043-5	95	5
4043-10	90	10
4043-15	85	15

The density of the samples has been determined by the Archimedes method using Mettler Toledo XS204 (Columbus, OH, USA) analytical balance equipped with density kit. The density of the PLA samples and their composites was tested with the aid of water (MiliQ water). Average values of density were determined for 10 readings. Theoretical density was calculated assuming the additivity of PLA density and DE true density  $\rho_{DE} = 2.227 \text{ g}\cdot\text{cm}^{-3}$  (see Supplementary Information (Tables S1 and S2)) as a weighted sum of both ingredients.

The melting and crystallization behavior of the PLA composites was studied under nitrogen atmosphere (purity 99.999) by differential scanning calorimetry using Q2000 DSC (TA Instruments, New Castle, DE, USA). Each sample of a mass of  $7.0 \pm 0.1 \text{ mg}$  was placed in an aluminum crucible ( $T_{\text{zero}}$ ) and held at a temperature of  $20 \text{ }^\circ\text{C}$  for 5 min. Following that, the sample was heated with a heating rate of  $10 \text{ K}\cdot\text{min}^{-1}$  to  $200 \text{ }^\circ\text{C}$  (ca.  $30 \text{ }^\circ\text{C}$  above the PLA matrix melting point of  $170 \text{ }^\circ\text{C}$ ) which represents the first heating run. The sample was held 5 min at  $200 \text{ }^\circ\text{C}$  and quenched. After quenching, the sample was held isothermally at  $20 \text{ }^\circ\text{C}$  for 5 min. Subsequently, the sample was heated with a heating rate of  $10 \text{ K}\cdot\text{min}^{-1}$  to  $100 \text{ }^\circ\text{C}$  (second heating run). The cold crystallization enthalpy ( $\Delta H_c$ ), maximum temperature peak of cold crystallization ( $T_c$ ), melting enthalpy ( $\Delta H_m$ ) and the maximum temperature peak of melting ( $T_m$ ) were obtained from the second first heating, the midpoint of the glass transition temperature ( $T_g$ ) and change in the heat capacity ( $\Delta C_p$ ) were obtained from the second heating run. The degree of crystallinity ( $X_c$ ) was estimated using the following equation:

$$X_c = \frac{\Delta H_m - \Delta H_c}{\Delta H_{m100\%}} \cdot 100\%, \quad (1)$$

with  $\Delta H_{m100\%} = 93.7 \text{ J}\cdot\text{g}^{-1}$  presented by Quero et al. [13]. Melting enthalpy was corrected for filler content ( $\omega$ ).

Static tensile test was carried out according to ISO 527-2:2012 using a Zwick/Roell Z005 (Ulm, Germany) electromechanical testing machine equipped with a load cell with a range of  $\pm 1 \text{ kN}$ . The test was controlled by a constant displacement of the grips, equal to  $15 \text{ mm}\cdot\text{min}^{-1}$ . The initial separation between the grips of the testing machine was  $90 \text{ mm}$ . A long-range extensometer was used of  $40 \text{ mm}$ . Average values of parameters were determined for at least five tests. Samples for the static tensile tests had a round beam shape with diameter ca.  $2 \text{ mm}$ , total length of  $90 \text{ mm}$ , whereas the measuring length of the extensometer was  $50 \text{ mm}$ .